Title

Integrin-mediated traction force enhances paxillin molecular associations and adhesion dynamics that increase the invasiveness of tumor cells into a three-dimensional extracellular matrix.

Journal

Molecular biology of the cell, 28(11)

ISSN

1059-1524

Authors

Mekhdjian, Armen H
Kai, FuiBoon
Rubashkin, Matthew G
et al.

Publication Date

2017-06-01

DOI

10.1091/mbc.e16-09-0654

Peer reviewed

Integrin-mediated traction force enhances paxillin molecular associations and adhesion dynamics that increase the invasiveness of tumor cells into a three-dimensional extracellular matrix

Armen H. Mekhdjian[a,†], FuiBoon Kai[b,†], Matthew G. Rubashkin[b,†], Louis S. Prahl[c], Laralynne M. Przybyla[b], Alexandra L. McGregor[d], Emily S. Bell[d], J. Matthew Barnes[b], Christopher C. DuFort[b], Guanqing Ou[b], Alice C. Chang[a], Luke Cassereau[b], Steven J. Tan[a], Michael W. Pickup[b], Jonathan N. Lakins[b], Xin Ye[e], Michael W. Davidson[f], Jan Lammerding[d], David J. Odde[c], Alexander R. Dunn[a,*], and Valerie M. Weaver[b,g,*]

[a]Department of Chemical Engineering, Stanford University, Stanford, CA 94305; [b]Center for Bioengineering and Tissue Regeneration, Department of Surgery, and [g]Departments of Anatomy, Bioengineering and Therapeutic Sciences, and Radiation Oncology, Eli and Edythe Broad Center of Regeneration Medicine and Stem Cell Research, and UCSF Helen Diller Comprehensive Cancer Center, University of California, San Francisco, San Francisco, CA 94143; [c]Department of Biomedical Engineering, University of Minnesota, Minneapolis, MN 55455; [d]Nancy E. and Peter C. Meinig School of Biomedical Engineering and Weill Institute for Cell and Molecular Biology, Cornell University, Ithaca, NY 14853; [e]Whitehead Institute for Biomedical Research, Cambridge, MA 02142; [f]National High Magnetic Field Laboratory and Department of Biological Science, Florida State University, Tallahassee, FL 32306

ABSTRACT **Metastasis requires tumor cells to navigate through a stiff stroma and squeeze through confined microenvironments. Whether tumors exploit unique biophysical properties to metastasize remains unclear. Data show that invading mammary tumor cells, when cultured in a stiffened three-dimensional extracellular matrix that recapitulates the primary tumor stroma, adopt a basal-like phenotype. Metastatic tumor cells and basal-like tumor cells exert higher integrin-mediated traction forces at the bulk and molecular levels, consistent with a motor-clutch model in which motors and clutches are both increased. Basal-like nonmalignant mammary epithelial cells also display an altered integrin adhesion molecular organization at the nanoscale and recruit a suite of paxillin-associated proteins implicated in invasion and metastasis. Phosphorylation of paxillin by Src family kinases, which regulates adhesion turnover, is similarly enhanced in the metastatic and basal-like tumor cells, fostered by a stiff matrix, and critical for tumor cell invasion in our assays. Bioinformatics reveals an unappreciated relationship between Src kinases, paxillin, and survival of breast cancer patients. Thus adoption of the basal-like adhesion phenotype may favor the recruitment of molecules that facilitate tumor metastasis to integrin-based adhesions. Analysis of the physical properties of tumor cells and integrin adhesion composition in biopsies may be predictive of patient outcome.**

Monitoring Editor
Alpha Yap
University of Queensland

Received: Sep 12, 2016
Revised: Mar 24, 2017
Accepted: Mar 29, 2017

This article was published online ahead of print in MBoC in Press (http://www.molbiolcell.org/cgi/doi/10.1091/mbc.E16-09-0654) on April 5, 2017.

†These authors contributed equally.

The authors declare no conflicts of interest.

*Address correspondence to: Valerie M. Weaver (Valerie.Weaver@ucsf.edu), Alexander R. Dunn (alex.dunn@stanford.edu).

Abbreviations used: AFM, atomic force microscopy; 3B, Bayesian analysis of bleaching and blinking; ECM, extracellular matrix; EMT, epithelial-to-mesenchymal transition; FA, focal adhesion; FAK, focal adhesion kinase; FRET, Förster resonance energy transfer; ILK, integrin-linked kinase; MEC, mammary epithelial cell; MTS, molecular tension sensor; PA, polyacrylamide; PINCH, particularly interesting new cysteine-histidine–rich protein; SAIM, scanning angle interference microscopy; TFM, traction force microscopy; TGFβ, transforming growth factor β.

INTRODUCTION

Metastasis is the main cause of death in patients with malignant tumors (Weigelt *et al.*, 2005; Johnson *et al.*, 2013; Lobbezoo *et al.*, 2015). Tumor metastasis proceeds through a series of critical steps that include invasion of malignant cells across the basement membrane and their directed migration into the parenchyma, where they form invasive carcinomas (Rowe and Weiss, 2008; Egeblad *et al.*, 2010). Thereafter, to metastasize, the malignant cells must migrate through the interstitial extracellular matrix (ECM) toward blood vessels and intravasate into the vasculature, where they can circulate as single cells, as cellular aggregates, or within fibrin-rich emboli (Massagué and Obenauf, 2016). Eventually, the disseminated "circulating" tumor cells either die or adhere to the capillaries of distal tissues, where they can extravasate. Once at the secondary site, the tumor cells must proliferate and recruit a new vasculature to form metastases (Nguyen *et al.*, 2009; Telerman and Amson, 2009; Chaffer and Weinberg, 2011). Each of these steps favors tumor cells that migrate efficiently through a dense, collagen- and fibronectin-rich ECM, as well as cells that are able to retain their viability during intravasation and extravasation—processes that demand considerable cellular and nuclear squeezing and distortion (Friedl and Wolf, 2003; Egeblad *et al.*, 2010; Roussos *et al.*, 2011; Bravo-Cordero *et al.*, 2012; Nguyen-Ngoc *et al.*, 2012; Denais *et al.*, 2016). Despite the clinical importance of metastasis and an appreciation of the physical hurdles that a tumor cell must overcome in order to disseminate, it remains unclear whether tumor cells exploit specific biophysical states or acquire unique mechanical properties to participate in the metastatic journey.

Cancer cell invasion and metastasis are influenced by the mechanical properties of the primary tumor and in particular the stiffness of the stromal ECM (Paszek *et al.*, 2005; Levental *et al.*, 2009; Pickup *et al.*, 2013; Bae *et al.*, 2014; Mouw *et al.*, 2014; Rubashkin *et al.*, 2014a; Acerbi *et al.*, 2015; Kai *et al.*, 2016). A stiffened ECM fosters malignant transformation and metastasis of mammary tissue in vivo and stimulates the invasion of human and murine mammary epithelial cells (MECs) in vitro (Paszek *et al.*, 2005; Levental *et al.*, 2009; Schedin and Keely, 2011; Pickup *et al.*, 2013; Rubashkin *et al.*, 2014a). The invasive front of human breast tumors is also stiffer, and the level of stiffness correlates with human breast tumor aggression (Acerbi *et al.*, 2015). These findings are consistent with the general observation that cells tune their cytoskeletal tension to the stiffness of their underlying ECM (Engler *et al.*, 2004; Discher *et al.*, 2005; Paszek *et al.*, 2005; Yeung *et al.*, 2005; Saha *et al.*, 2008; Butcher *et al.*, 2009; Allen *et al.*, 2012; Cosgrove *et al.*, 2014; Chaudhuri *et al.*, 2015). Invading tumor cells engage the ECM through integrins, a class of heterodimeric, transmembrane proteins that link the cytoskeleton to the surrounding ECM. In response to a stiff ECM, integrin receptors assemble into focal adhesions (FAs), micrometer-sized assemblies consisting of hundreds of proteins that, in addition to their mechanical roles, mediate signaling through multiple pathways (Hoffman *et al.*, 2011). Mechanically activated signaling via integrin-based adhesions not only enhances tumor cell growth and survival, but it also drives tumor cell invasion and migration (Jaalouk and Lammerding, 2009; DuFort *et al.*, 2011; Batra *et al.*, 2012; Carisey *et al.*, 2013; Ross *et al.*, 2013; Yao *et al.*, 2014; Rubashkin *et al.*, 2014b; Paluch *et al.*, 2015). Consistently, treatments that inhibit FA formation or that ablate FA signaling reduce cancer progression and metastasis (White *et al.*, 2004; Huveneers *et al.*, 2007; Provenzano *et al.*, 2008; Sulzmaier *et al.*, 2014; Winograd-Katz *et al.*, 2014). These observations support a picture in which a stiffened stroma, contractile cancer cell cytoskeleton, and integrin-dependent intracellular signaling combine to support cancer growth and metastasis. However, the colonization of distant metastasis sites requires passage through a series of narrow constrictions. This would seem to pose a contradiction because a stiffened tumor cell should have a distinct disadvantage when attempting to navigate confined microenvironments during the process of metastasis.

One plausible explanation that could link matrix mechanics, adhesion dynamics, and metastatic potential may reside in the observation that metastatic tumor cells often exhibit traits consistent with an epithelial-to-mesenchymal transition (EMT)—a developmental process that is often hijacked by cancer cells (Egeblad *et al.*, 2010; Taube *et al.*, 2010; Craene and Berx, 2013; Jung *et al.*, 2015). An EMT allows formerly epithelial cells to access a mesenchymal form of cell migration that conceivably facilitates cancer cell invasion within dense ECMs, permitting their efficient dissemination to form distant metastatic colonies (Chaffer and Weinberg, 2011; Craene and Berx, 2013; Lamouille *et al.*, 2014). Canonical EMT is characterized by expression of key transcriptional regulators, including Twist, Snail, and Slug, leading to a loss in cadherin-dependent cell–cell adhesion and apical-basal polarity and increased cell–ECM adhesion and matrix metalloproteinase (MMP) expression (Yilmaz and Christofori, 2009; Przybyla *et al.*, 2016). Moreover, whereas an EMT-like transition can be triggered by exposure to chemokines such as transforming growth factor β (TGFβ), it is also promoted by a stiff ECM that is located at the invasive front of tumors (Acerbi *et al.*, 2015; Wei *et al.*, 2015; Przybyla *et al.*, 2016).

Of importance, the idea that tumor cells require an EMT to metastasize and that this transformation is associated with reduced cortical tension has been questioned (Thoelking *et al.*, 2010; Buckley *et al.*, 2012; Schneider *et al.*, 2013; Fischer *et al.*, 2015; Zheng *et al.*, 2015). In some circumstances, metastasis is favored by tumor aggregates (Friedl *et al.*, 2012; Nguyen-Ngoc *et al.*, 2012; Cheung *et al.*, 2016). Furthermore, intravital imaging clearly illustrates that tumor cells can invade as cellular collectives (Gaggioli *et al.*, 2007; Hidalgo-Carcedo *et al.*, 2010; Manning *et al.*, 2015), a finding that accords well with the observation that metastatic cells often retain E-cadherin expression (Cheung *et al.*, 2013; Aceto *et al.*, 2014). A plausible alternative explanation for the apparently disparate theories that argue for either single EMT or collective tumor metastasis is that tumor cells may engage in a "partial" or "transient" EMT to disseminate (Chaffer and Weinberg, 2011; Jolly *et al.*, 2015, 2016). Consistent with this proposition, live-cell imaging of tumor aggregates with a high propensity to metastasize revealed that the leader "invading" cells exhibited a basal-epithelial phenotype (for convenience, "basal-like"), with features reminiscent of a partial EMT (Cheung *et al.*, 2013).

In summary, although evidence indicates that matrix mechanical properties can exert strong effects on cancer metastasis, the molecular mechanisms are poorly understood. In particular, whether a stiff ECM could foster tumor metastasis by inducing a "basal-like" or pseudo-EMT phenotype via mechanical, integrin-mediated signaling has yet to be determined. Moreover, whether this "basal-like switch" endows tumor cells with biophysical properties that potentiate the metastasis of the EMT-like cells and, if so, how, are not known. To investigate these possibilities, we interrogated the relationship between integrin adhesion dynamics, composition, and forces and the cellular biophysical properties that favor tumor cell invasion within a confined, stiffened three-dimensional (3D) ECM.

RESULTS

ECM stiffness stimulates tumor cell invasion and induces a basal-like phenotype

We first asked whether a stiffened tumor ECM could promote the metastatic behavior of mammary tumors by inducing a basal-like,

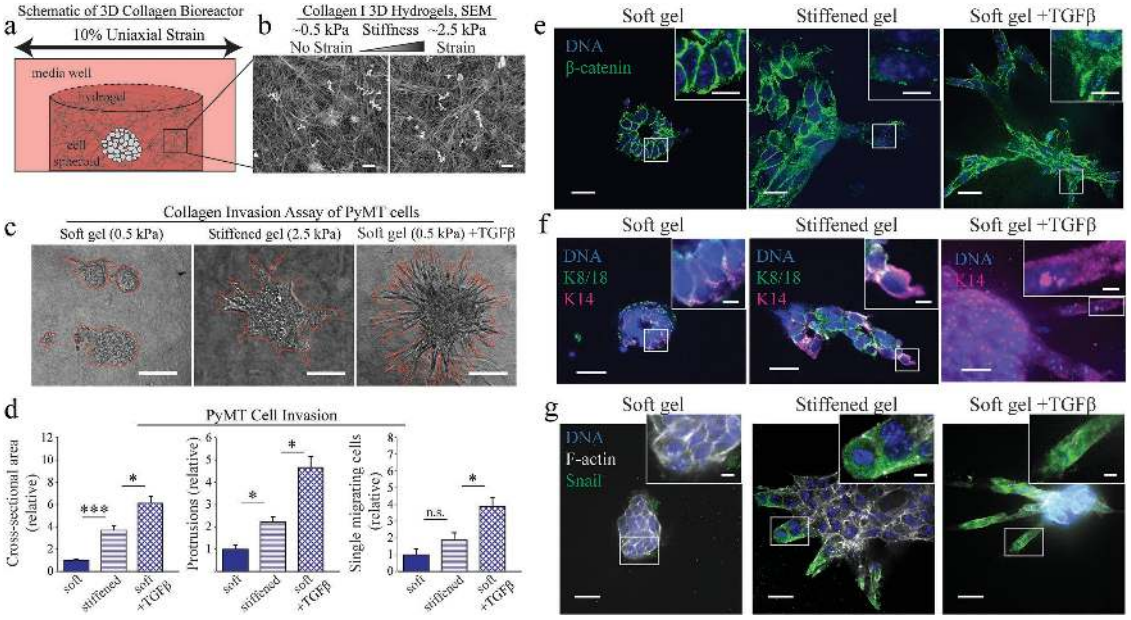

FIGURE 1: Tumorigenic cancer cells exhibit a basal-like phenotype that is fostered by ECM stiffness and EMT. (a) Schematic of the 3D collagen bioreactor. Collagen I hydrogels are made in a media reservoir as described previously (Cassereau *et al.*, 2015), and the application of 10% strain leads to an increase in effective gel stiffness from 0.5 to 2.5 kPa. (b) SEM images of representative 2.5 mg/ml collagen hydrogels in strained and unstrained conditions. Porosity and fiber orientation are unaltered at 10% strain; increased stiffness may reflect fiber bundling. Scale bar, 2 μm. (c) A 3D collagen invasion assay of multicellular spheroids composed of tumorigenic PyMT cells in 2.5 mg/ml 3D collagen gels that are unstrained (soft, 0.5 kPa) or strained (stiffened, 2.5 kPa) for 72 h. Tumorigenic PyMT cells recapitulate invasive behavior when induced to undergo EMT via treatment with TGFβ. Scale bar, 100 μm. (d) Quantification of invasion parameters, total cross-sectional area of spheroid and protrusions, number of protrusions, and number of migrating cells normalized to the unstrained, untreated condition. Mean ± SEM (*$p < 0.05$; ***$p < 0.001$; >20 cells). (e) Immunofluorescence imaging of PyMT cell spheroids in 3D collagen gel stained for β-catenin (green) and DNA (DAPI, blue). β-Catenin strongly localizes to cell–cell junctions in cells cultured in soft 3D gels, whereas it is found more diffusely within the cytoplasm and nucleus in strain-stiffened gels and TGFβ-treated cells. (f) PyMT cell spheroids in a 3D collagen bioreactor express basal epithelial marker K14 at the leader cells when cultured in strain-stiffened gels but maintain luminal epithelial K8/18 in the noninvasive core. Induction of EMT via TGFβ treatment also leads to expression of K14 in leader cells. (g) Snail transcription visualized by Snail-YFP is up-regulated in leader cells in strain-stiffened gels and TGFβ-treated cells. Scale bar, 50 μm (e–g), 10 μm (inset).

invasive phenotype (Pickup *et al.*, 2013). We examined the behavior of mouse tumor colonies (Borowsky *et al.*, 2005) generated by growing mammary epithelial cell (MEC) PyMT tumor cells within a reconstituted basement membrane (rBM; 3–5 d) to form colonies, followed by their embedment within a 3D collagen/fibronectin bioreactor (72 h), where they were either maintained without modification or subjected to uniaxial stretch (10%; 72 h). The uniaxial stretch induces local strain stiffening of the collagen gel, increasing its stiffness fivefold (from ~0.5 to ~2.5 kPa) without altering bulk ECM concentration or pore size (Cassereau *et al.*, 2015; Figure 1, a and b). Phase contrast images of colonies 72 h after their embedment and manipulation showed that the PyMT tumor colonies within the soft collagen/fibronectin gels exhibited little to no invasion. However, PyMT tumor colonies subjected to a stiffened ECM invaded significantly, although not to the same extent as those treated with TGFβ to induce an EMT (Figure 1, c, and quantified in d). On further investigation, confocal images revealed that the PyMT colonies within the soft (~0.5 kPa) collagen/fibronectin hydrogels retained their epithelial phenotype, as indicated by β-catenin localization to cell–cell junctions, maintenance of cortical actin organization, and intense cytokeratin K8/18 expression (Figure 1, e and f, and Supplemental Figure S1). In contrast, the PyMT MECs invading into the stiffened ECM gels exhibited hallmarks of a basal-like phenotype. This basal-like phenotype included loss of junctional β-catenin, reorganization of actin into linearized bundles parallel to the axis of invasion, and acquisition of cytokeratin K14 in the leader cells, reminiscent of, but not identical to, the PyMT MECs that had undergone an EMT in response to TGFβ (Figure 1, e and f, and Supplemental Figure S1). Furthermore, expression of a knock-in IRES (internal ribosomal entry site) yellow fluorescent protein (YFP) Snail reporter (Ye *et al.*, 2015) indicated that only the invading PyMT leader cells within the stiff gels had abundant Snail transcripts that approximated the level uniformly expressed by all cells in PyMT colonies that had undergone a complete EMT (Figure 1g). These findings are consistent with the idea that a stiffened ECM could promote tumor metastasis by inducing a basal-like or partial EMT phenotype.

Metastatic tumor cells and tumor cells with a basal-like phenotype exhibit enhanced invasion within confined spaces

A prerequisite for tumor metastasis is the efficient migration of tumor cells through a dense and stiffened ECM, followed by their intravasation into the vasculature and extravasation into the metastatic site. These behaviors would plausibly be favored by more-compliant cells, as predicted to be exhibited by cells with either a basal or a mesenchymal phenotype after EMT (Sahai, 2007;

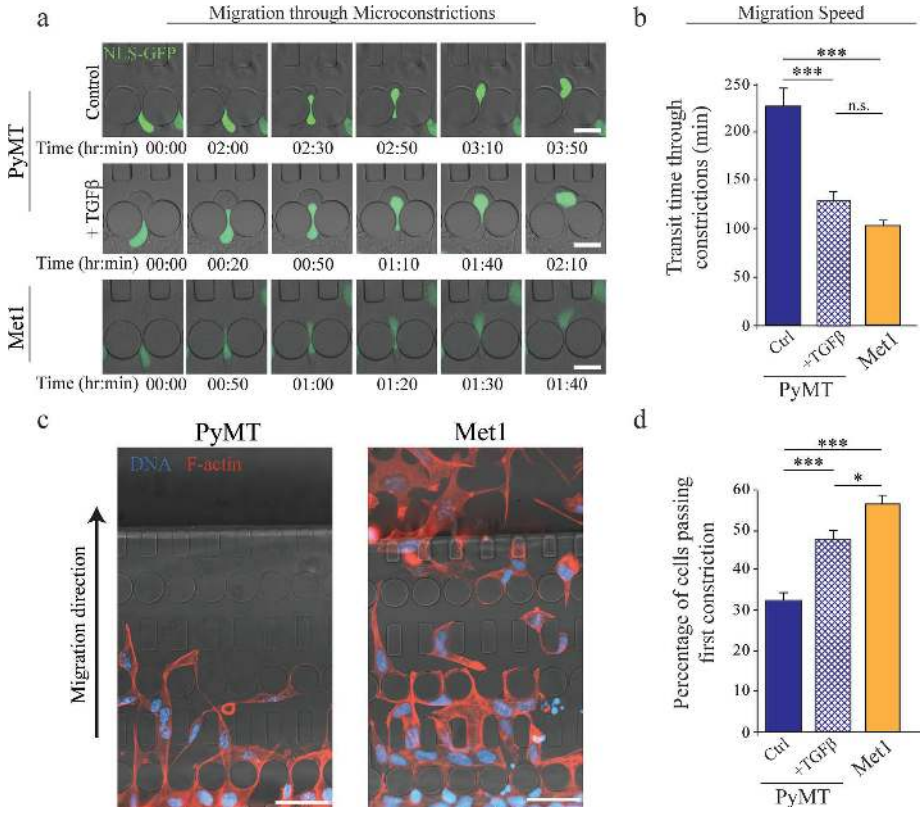

FIGURE 2: Cells with a basal phenotype display enhanced migration through microconstrictions. (a) Representative time-lapse image sequences of PyMT cells, PyMT cells treated with TGFβ, and Met1 cells migrating through a 1×5 μm^2 constriction inside a microfluidic device. Cells express NLS-GFP to visualize the nucleus. Time displayed as hours:minutes. Scale bar, 20 μm. (b) Transit times for cell passage through constrictions ≤10 μm^2 in cross-sectional area, demonstrating that both Met1 cells and PyMT cells treated with TGFβ migrate faster through the small constrictions. Mean ± SEM (*$p < 0.05$, ***$p < 0.001$, by Kruskal–Wallis test with Dunn's multiple comparisons; >70 cells from three independent experiments). (c) Representative images of cells inside the microfluidic devices after 48 h of confined migration. Fixed cells were stained for F-actin (phalloidin) and DNA (Hoechst 33342). Scale bar, 50 μm. (d) Incidence of cells successfully migrating through the first row of constrictions within 36 h relative to the total number of cells inside the microfluidic channels. Error bars represent SE of the binomial distribution (*$p < 0.05$; ***p <0.001; >500 cells by Fisher's exact test with Bonferroni correction).

Swaminathan *et al.*, 2011; McGrail *et al.*, 2015). To test this idea, we examined the migration of PyMT tumor MECs through constricted microchannels that mimic the confined, stiff microenvironment through which metastasizing tumor cells would likely navigate (Davidson *et al.*, 2015; Denais *et al.*, 2016; Figure 2). We compared cell behaviors after induction of EMT by treatment with TGFβ to that of Met1 MECs, a PyMT variant that was previously shown to exhibit a propensity to metastasize and yet retain epithelial-like characteristics (Borowsky *et al.*, 2005; Qian *et al.*, 2011). TGFβ-treated PyMT MECs migrated more efficiently than untreated MECs through the confined channels, as indicated by significantly shorter transit times through the constrictions (Figure 2, a and b) and higher percentages of cells migrating through constrictions with a cross-sectional area of <10 μm^2 (Figure 2, c and d). Of importance, Met1 tumor MECs migrated as efficiently as the TGFβ-treated PyMT tumor MECs, implying that complete EMT is not a prerequisite for efficient migration through a confined space.

Because cells with increased mechanical deformability pass more easily through confined spaces, we concluded that it was possible that increased migration of TGFβ-treated PyMT MECs and Met1 MECs was due to altered cytoskeletal mechanical deformability. To test this idea, we used atomic force microscopy (AFM) to measure the average cortical elasticity of multiple tumor cells plated on 2.7-kPa gels, using a 5-μm bead-ligated cantilever with multiple indentations across the cellular surface (Figure 3a). The resulting force–indentation curves were fit to a Hertz model to estimate an effective elastic modulus (Figure 3b). Consistent with the notion that tumor cells with a higher propensity to metastasize are more compliant (Swaminathan *et al.*, 2011), our AFM measurements revealed that the Met1 MECs had a modest but significant reduction in effective stiffness compared with the PyMT MECs (Figure 3, c and e). Nevertheless, the compliance of the EMT-induced PyMT MECs was similar to that of the less invasive, untreated PyMT MECs (Figure 3, c and e).

Another component of cellular deformability that modulates cell migration through a confined microenvironment is nuclear stiffness (Davidson *et al.*, 2014; Harada *et al.*, 2014; Lautscham *et al.*, 2015; Denais *et al.*, 2016). Micropipette aspiration experiments indicated that there was a modest but statistically significant increase in nuclear deformability in the EMT-induced PyMT MECs (Figure 3, f and g). The findings are consistent with the argument that an EMT increases nuclear deformability and not cortical stiffness to facilitate cell migration through confined spaces and that this could potentiate tumor metastasis.

Tumor cells that migrate more efficiently within a confined space are more contractile

We next explored whether the enhanced invasive phenotype observed by the metastatic and EMT-induced MECs in the confined channels was associated with differences in cell–ECM interactions, as measured by the degree of cell spreading and/or traction force generation. We used traction force microscopy (TFM; Munevar *et al.*, 2001; Paszek *et al.*, 2005) and compared traction forces exerted by the Met1 and the untreated versus EMT-induced PyMT tumor MECs plated on fibronectin-conjugated polyacrylamide (PA) gels with a stiffness calibrated to mimic that measured at the invasive front of the malignant human and murine mammary tissue stroma (~2.7 kPa; Munevar *et al.*, 2001; Paszek *et al.*, 2005; Laklai *et al.*, 2016). We observed that both the TGFβ-treated PyMT MECs and the Met1 MECs generated higher maximal and total cellular traction forces (Figure 4, a, and quantified in b) and higher spread area (unpublished data). We also measured higher total and maximal adhesion traction forces and enhanced cell spreading in premalignant human MCF10AT MECs induced to undergo EMT by treatment with TGFβ as compared with their nontreated controls (Figure 4, c, and quantified in d). As expected, TGFβ-treated MCF10ATs also spread progressively more on hydrogel surfaces functionalized with increasing concentrations of fibronectin (Supplemental Figure S2).

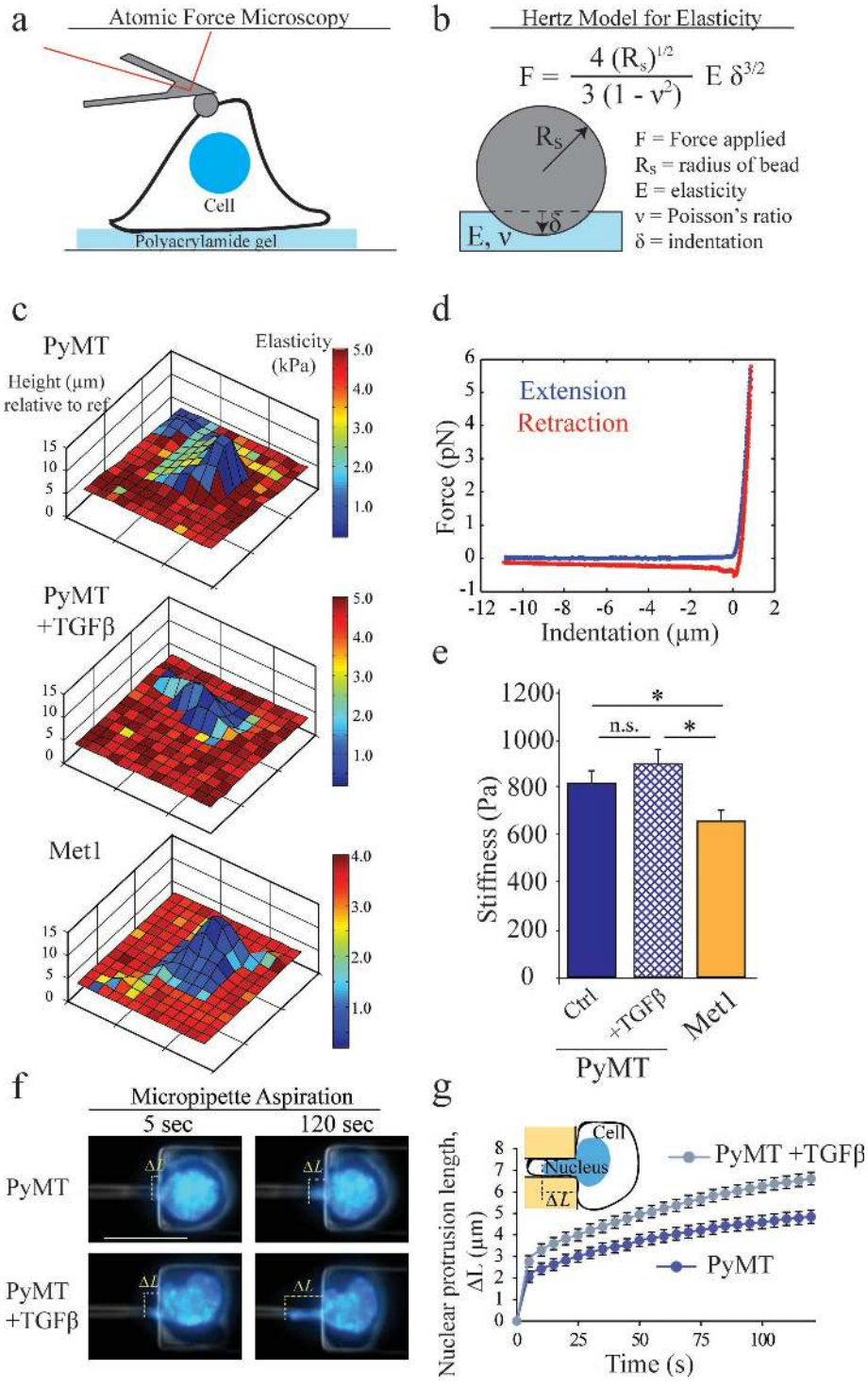

FIGURE 3: Cells with a basal phenotype are mechanically more compliant. (a) Schematic of AFM used to measure effective cell stiffness. Cells are seeded on a 2.7-kPa PA gel conjugated with fibronectin and indented using a 2.5-μm beaded tip on the AFM cantilever. (b) Hertz model and parameters used to estimate elasticity from a bead contacting a flat plane. (c) Representative example surface plots of elasticity for PyMT, TGFβ-treated PyMT, and Met1 cells, showing elasticity as function of cell topology. (d) Representative force–indentation curves for a given pixel in the surface map, showing the extension and retraction of the cantilever. The Hertz model is fit to these data to extract an effective cell elasticity. (e) Quantification of cell indentation stiffness for tumorigenic PyMT cells, with and without TGFβ treatment, and metastatic Met1 cells. Met1 cells are modestly softer on average than PyMT cells, with TGFβ treatment not eliciting a statistically significant response. Mean ± SEM (*$p < 0.05$; >15 cells). (f) Micropipette aspiration of PyMT and TGFβ-treated PyMT cells showing the deformation of the nucleus over time. Cell nuclei were visualized by staining DNA with Hoechst 33342. (g) Compiled nuclear protrusion length (ΔL) as a function of time, indicating some nuclear softening in response to TGFβ treatment. Mean ± SEM (>120 cells from three independent experiments). Scale bar, 20 μm.

Cells that underwent EMT frequently increase $\alpha_5\beta_1$ integrin expression, and fibronectin-ligated $\alpha_5\beta_1$ integrin can significantly enhance cell spread area and cell–ECM traction force (Mierke *et al.*, 2011; Lamouille *et al.*, 2014). Consistently, immunoblot and fluorescence-activated cell sorting (FACS) revealed more total and cell surface α_5 integrin expression in the TGFβ-treated MCF10A and PyMT MECs (unpublished data). To determine whether higher α_5 integrin expression could account for the observed gain in cell spreading and traction force generation observed in the TGFβ-treated MECs, we engineered MCF10A MECs to ectopically express higher total α_5 integrin. After confirming more than a two-fold increase in cell surface α_5 integrin expression by FACS, we assayed for cell spread area and traction force compared with paired control and TGFβ-treated MCF10A MECs. Whereas the MCF10A MECs expressing higher levels of α_5 integrin spread more and exerted higher traction force in response to a fibronectin gel, the magnitude of the increase was significantly lower than that after induction of EMT by TGFβ treatment (Supplemental Figure S3).

In summary, these findings suggest that in addition to an increase in nuclear deformability, there may also be an association between the ability of cells to exert higher cell–ECM traction forces and their ability to migrate more efficiently through a confined microenvironment. The data also argue that this phenotype cannot be solely explained by differences in integrin heterodimer expression.

Motor-clutch model of cellular traction predicts higher force and cell spread area for cells that have an enhanced ability to migrate within a confined space

We next used computational modeling to explore the interplay between cell adhesion and cell-generated traction forces exerted on compliant substrates. We first modified an existing computational motor-clutch model of cellular traction generation on compliant substrates (Chan and Odde, 2008). In this model, myosin motors slide an F-actin bundle and transmit forces to a compliant substrate through physical extension of molecular "clutch" molecules that

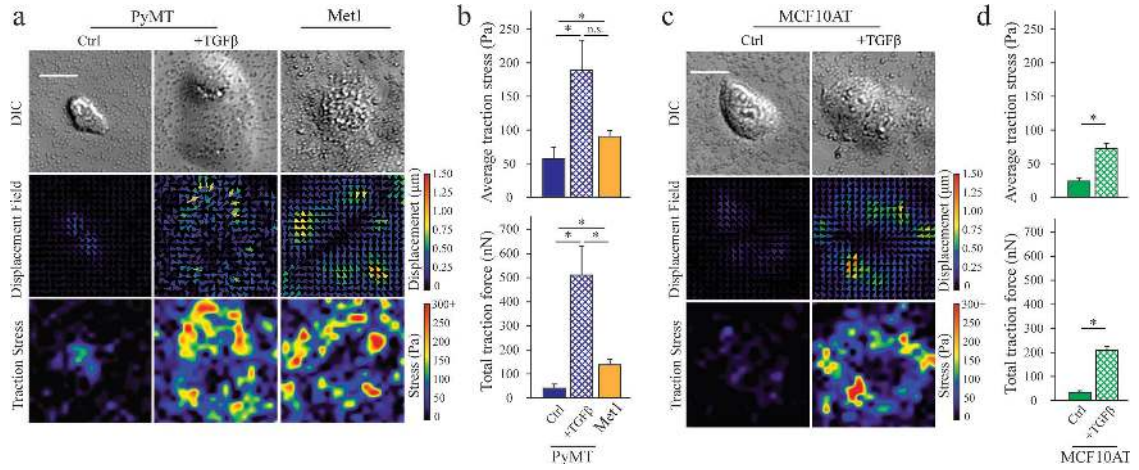

FIGURE 4: Cells with a basal phenotype exert higher traction forces. (a) PyMT and Met1 cells were seeded on 2.7-kPa PA gels conjugated with fibronectin and embedded with fluorescent beads for TFM. The displacement fields reflect the relative positions of beads before and after cell lysis. At a substrate stiffness comparable to that of tumor ECM (~2.7 kPa), Met1 cells are more spread and exert more traction forces on the substrate. Induction of EMT in PyMT cells by treatment with TGFβ recapitulates the increase in traction forces observed with Met1 cells, with total traction force even greater than for the Met1 cells. (b) Quantification of cell traction parameters. Metastatic cells have significantly increased total cellular and maximum traction forces. Mean ± SEM (*$p < 0.05$; >5 cells). (c) TFM of MCF10ATs. Cells that undergo TGFβ-induced EMT exert higher traction forces than untreated cells. (d) Quantification of cell traction parameters. TGFβ-treated MCF10ATs have significantly higher traction forces. Mean ± SEM (*$p < 0.05$; >5 cells). Scale bar, 20 μm (a, c).

transiently engage the actin filament (Figure 5a). The model revealed that efficient force transmission depends on the number and biophysical properties of the motors and clutches, clutch binding and force-dependent unbinding rates, and substrate mechanical properties (Figure 5b; Bangasser *et al.*, 2013). Maximal force transmission occurs at an "optimum" substrate stiffness, whereas clutch unbinding increases on softer or stiffer substrates, leading to inefficient force transmission (Bangasser *et al.*, 2013). Actin retrograde flow is biphasic and inversely correlated with traction force, and a leading-edge protrusion rate can be used as a proxy for spread area, defined by the difference between protrusion and retrograde flow (Chaudhuri *et al.*, 2015).

Simulated cells with larger numbers of both myosin II motors and integrin-mediated adhesion clutches are better spread and generate larger tractions on surfaces with increasing stiffness but then go through a maximum so that at even higher stiffness, area and force are decreased (Figure 5, c and d). The prediction of increasing area and force is consistent with the larger adhesion sizes and increased traction generation observed for Met1 MECs and TGFβ-treated PyMT and MCF10AT MECs relative to untreated PyMT and MCF10AT cells (Paszek *et al.*, 2005), at least below the optimal stiffness. Within the stiffness range of ~0.1–10 kPa, our results are consistent with nontransformed MECs employing a "weak clutch" regime. In this regime, an imbalance of contractile force and clutch number results in a failure to spread and low traction forces that modestly increase near disease-level stiffness. On addition of TGFβ and induction of an EMT phenotype, the simulated MECs express larger numbers of both motors and integrin-mediated adhesions and shift to a "balanced motor-clutch" regime in which the clutch strength matches that of the motors, resulting in slower actin flow, enhanced cell spreading, and higher traction forces (Figure 5, c and d).

As previously described (Chan and Odde, 2008; Bangasser *et al.*, 2013), the motor-clutch model predicts a decrease in cell spread area and traction force at a substrate stiffness extending beyond an optimum stiffness (here ~10 kPa for TGFβ-treated MCF10As). By contrast, many cell types remain well spread and generate large traction forces even on stiff substrates (Ghibaudo *et al.*, 2008; Elosegui-Artola *et al.*, 2014, 2016). We developed a modified motor-clutch model that includes force-dependent recruitment of adhesion components in response to substrate stiffness, similar to recently proposed models (Elosegui-Artola *et al.*, 2014, 2016). Briefly, we incorporated a clutch recruitment feedback rate (k_{add}), which is proportional to the number of clutches experiencing force above a threshold ($F_{threshold}$), as well as a maximum number of clutches available to be recruited ($n_{clutch,max}$; see the Supplemental Material for model description). By varying key parameters within the feedback response (in particular, k_{add}), we recapitulate varying degrees of reinforcement on stiff substrates, with higher reinforcement values (k_{add} = 0.1–1 s^{-1}), yielding a monotonic trend (Supplemental Figure S4). Hence our PA gel results alone did not provide enough information to distinguish between the two models—either TGFβ-treated cells have a higher optimum stiffness due to increased motor and clutch number, or our results are consistent with engaging adhesion reinforcement on stiff substrates.

Cells with a basal-like phenotype exert higher integrin-dependent force

To explore the model predictions further, we tested whether the increased overall cellular traction forces observed in Met1 and TGFβ-treated PyMT and MCF10A MECs translated into an increase in molecular forces at the level of individual adhesion complexes. To do so, we employed molecular tension sensors (MTSs), which report the forces exerted on integrin molecules in living cells (Morimatsu *et al.*, 2013, 2015; Chang *et al.*, 2016). Briefly, this technique incorporates an elastic protein spring flanked by two fluorophores that form a FRET pair (Figure 6a). The MTSs have an integrin-recognition domain containing the linear RGD tripeptide, which binds fibronectin-binding integrins. When cells adhere specifically via their integrins to an MTS-coated substrate, tension on individual sensors causes the elastic protein to stretch and the fluorophores to move

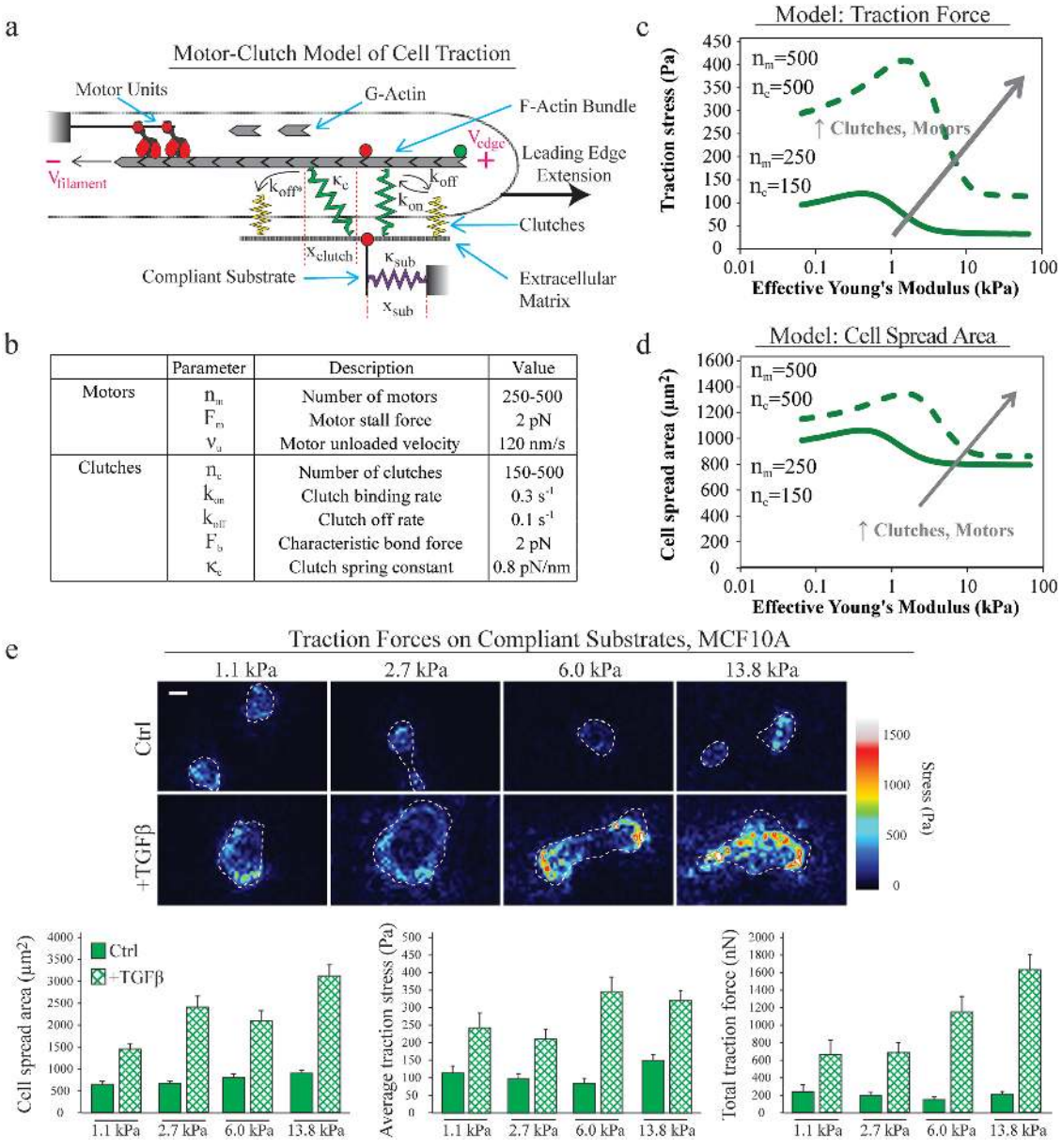

	Parameter	Description	Value
Motors	n_m	Number of motors	250-500
	F_m	Motor stall force	2 pN
	v_u	Motor unloaded velocity	120 nm/s
Clutches	n_c	Number of clutches	150-500
	k_{on}	Clutch binding rate	0.3 s^{-1}
	k_{off}	Clutch off rate	0.1 s^{-1}
	F_b	Characteristic bond force	2 pN
	κ_c	Clutch spring constant	0.8 pN/nm

FIGURE 5: Motor-clutch model of cellular traction predicts higher force and spread area for cells with a basal phenotype. (a) Motor-clutch model of cell traction, including myosin contractility, actin assembly/treadmilling/disassembly, clutches (linear elastic springs) with constant k_{on} and variable k_{off} rates (dependent on clutch strain, x_{clutch}), and a linear elastic compliant substrate. (b) Parameter descriptions and values used in motor-clutch simulations. (c) Model predictions of traction force calculated from the results of the simulation. Increasing number of motors and clutches leads to an increase in traction force with substrate stiffness and shifts the peak traction to a higher stiffness. (d) Model predictions of cell adhesion area that is extrapolated from the length of assembled filaments, which in turn depends on the number of motors and clutches. (e) TFM of MCF10A cells with and without TGFβ treatment seeded on PA gels of varying stiffness. Cell spread area was quantified from bright-field images, average stress was calculated from the displacement fields, and total force was quantified by multiplying average traction stress by the spread area of the cell (>10 cells). The total force values represent the sum of individual pixel forces underneath the cell body as a whole (average stress times spread area). Scale bar, 20 μm.

farther apart, yielding a decreased fluorescence resonance energy transfer (FRET) signal. An average force exerted on an ensemble of sensors within a given pixel is then calculated using a previously determined calibration curve (Grashoff *et al.*, 2010) modified to incorporate the specific fluorophores used in these studies (Figure 6b).

Using this approach, we found that both the TGFβ-treated PyMT MECs and the metastatic Met1 MECs generated higher total forces at their integrins than did the untreated PyMT MECs, consistent with the TFM data (Figure 4). In addition, both the Met1 MECs and the TGFβ-treated PyMT tumor MECs exhibited a modest but statistically significant increase in the average force per MTS sensor (Figure 6, c, and quantified in d). This integrin-force phenotype appears to be conserved: MCF10As that had undergone a TGFβ-induced EMT also spread more, assembled larger adhesions, generated higher total tractions as measured using MTSs, and exhibited a modest but consistent increase in the force per MTS compared

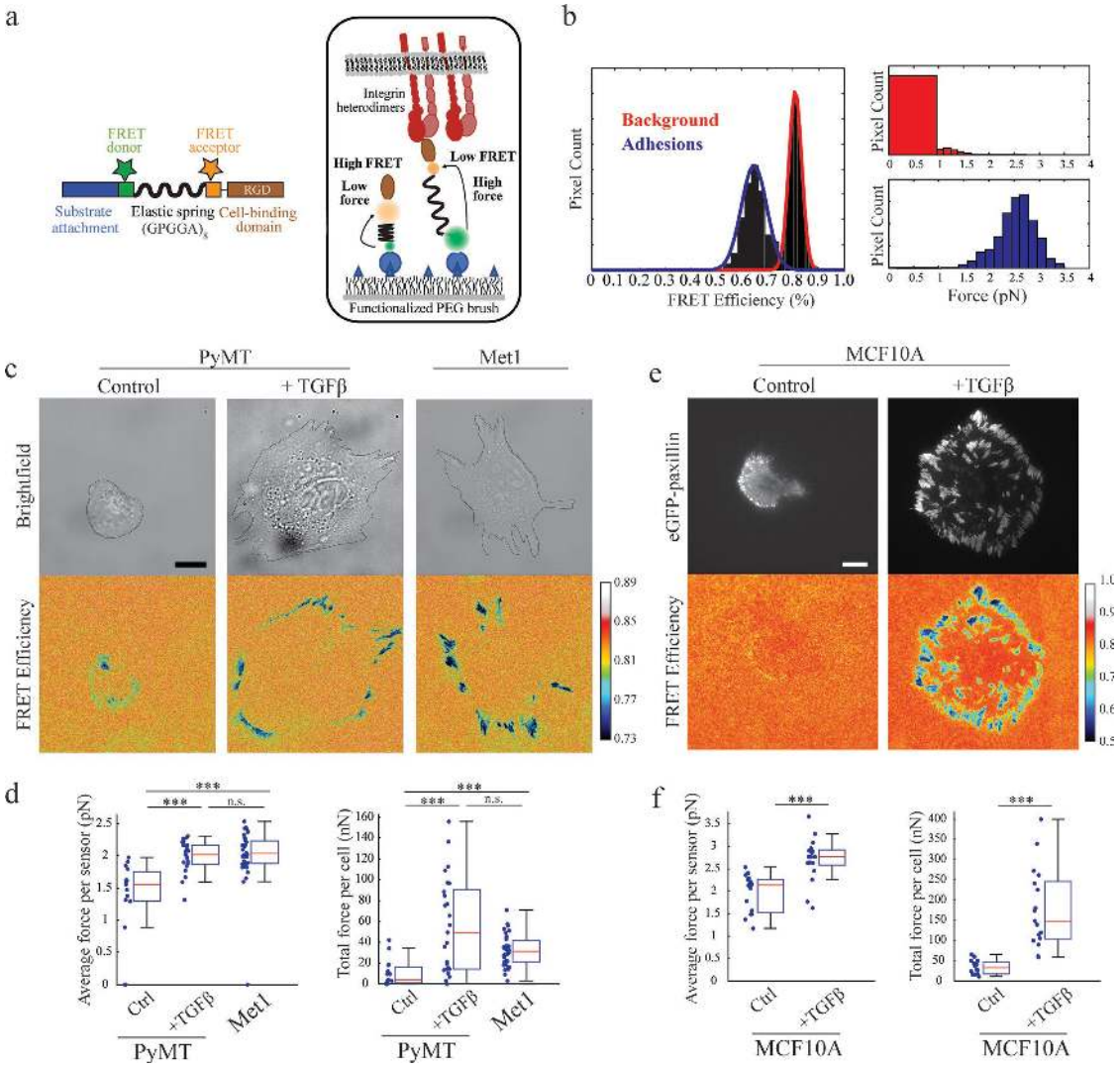

FIGURE 6: Cells with a basal phenotype exert higher integrin-dependent force. (a) Schematic of integrin MTSs. (b) FRET efficiency is converted into force using a calibration curve previously determined (Grashoff *et al.*, 2010) and modified for the fluorescent dyes used here. (c) When seeded on a coverslip densely coated with MTSs, Met1 cells and TGFβ-treated PyMT cells spread more readily and generate higher integrin-mediated forces than untreated PyMT cells. (d) Quantification of the total force and average force per integrin MTS, which are both higher for Met1 than with PyMT cells. TGFβ treatment of PyMT cells resulted in an increase in cell spread area (unpublished data), total integrin-mediated force per cell, and average force per MTS, similar to the values measured for Met1 cells (***$p < 0.001$; >15 cells by the Wilcoxon rank sum test). Box-and-whisker plots display the median (red), 25th and 75th percentiles (bottom and top edges of the box, respectively), and the most extreme data points not considered outliers (edge of whiskers). (e) Integrin MTS measurements for MCF10A cells treated with TGFβ. (f) There is an increase in total force and average force for the TGFβ-treated MCF10As compared with the untreated ones (***$p < 0.001$; >15 cells by the Wilcoxon rank sum test). In d and f, the total force values represent the sum of individual pixel forces specifically within segmented adhesions. Scale bar, 10 μm (c, e).

with untreated MCF10A MECs (Figure 6, e, and quantified in f). Note that the forces reported in Figure 6 are calculated specifically within adhesions; analyzing the MTS sensor data in a similar manner as the TFM data (namely, by including all pixels underneath the cell body) yields similar magnitudes of total force between the two techniques (Supplemental Figure S5; Chang *et al.*, 2016). Because the MTS substrates are effectively much stiffer than PA gels, we used this to test the reinforcement-model prediction that total traction forces and spread areas for TGFβ-treated cells remain uniformly high on stiff substrates. Of interest, contrary to this prediction, TGFβ-treated cells show lower traction forces and reduced spread area on the MTS substrates compared with 13.8-kPa gels (Supplemental Figure S5), consistent with cells adhering to surfaces that are stiffer than their optimal stiffness (Bangasser *et al.*, 2013). In addition, whereas the increased force per bond is statistically significant, it is relatively modest compared with the increase in overall traction force (Figure 6, c–f), implying that the number of motors and clutches both increased. Therefore we conclude that the results are consistent with a model in which EMT transition induces an increase in both motors and clutches while also shifting from a "weak clutch" regime to "balanced motor-clutch" regime (as in Figure 5, c and d) but are inconsistent with a model that relies entirely on a force-feedback reinforcement mechanism (as in Supplemental Figure S4, c and d).

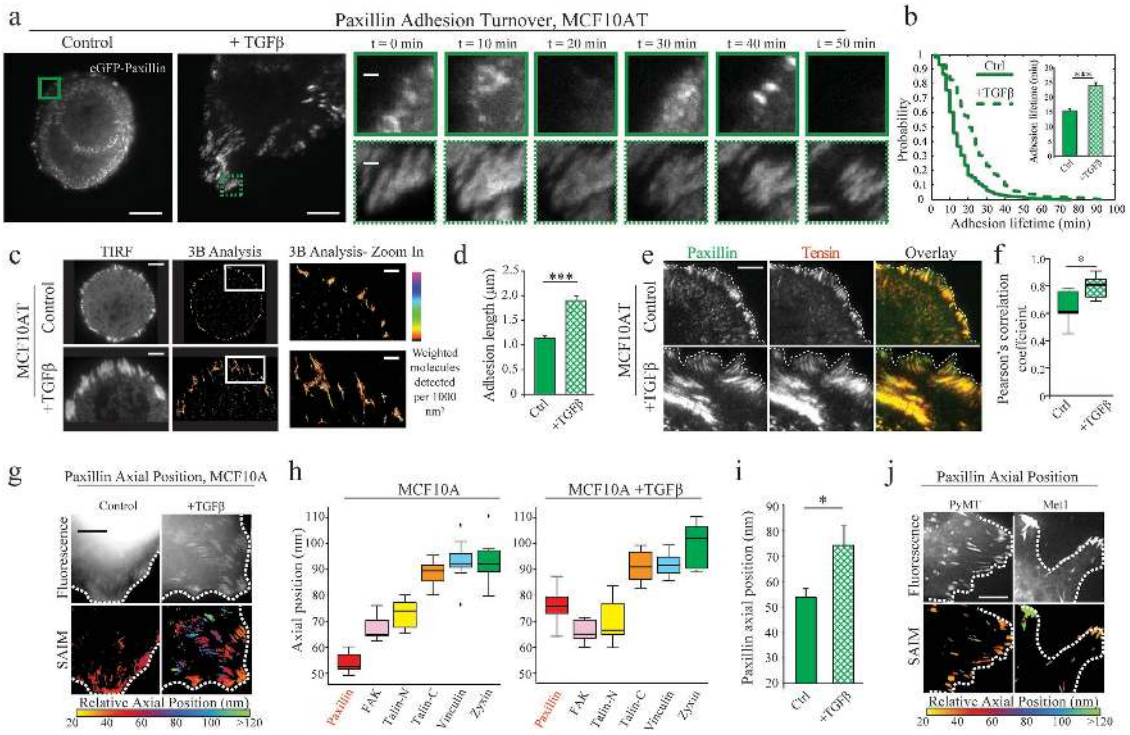

FIGURE 7: TGFβ-induced EMT alters adhesion organization and stability. (a) Live-cell imaging of paxillin-mEmerald and tensin-mCherry to visualize focal adhesion turnover in MCF10AT cells with and without TGFβ treatment. Top row: control, bottom row: TGFβ-treated. Scale bar, 10 μm (main image), 1 μm (inset). (b) Cumulative distributions of adhesion lifetimes. Inset, quantification of mean adhesion lifetime; mean ± SEM (***$p < 0.001$; >150 adhesions from five cells total). (c) Focal adhesion microstructure of MCF10AT seeded on MTSs overexpressing paxillin-eGFP and imaged with TIRF and 3B superresolution microscopy. Scale bar, 3 μm (main image), 1 μm (zoom). (d) Quantification of mean adhesion length of MCF10AT cells. TGFβ-treated cells have significantly longer adhesions; mean ± SEM (***$p < 0.001$; >100 adhesions from five cells). (e) Tensin-positive fibrillar adhesion formation in MCF10AT overexpressing paxillin-mEmerald and tensin-mCherry. Scale bar, 3 μm. (f) Quantification of the spatial colocalization between tensin and paxillin in adhesions. TGFβ-treated cells have significantly more paxillin-tensin colocalization (*$p < 0.05$; >10 cells). Pearson's correlation was calculated based on pixels within the focal adhesion areas. (g) Paxillin-mEmerald (N-terminal) axial position in focal adhesions in MCF10As measured with SAIM. Paxillin position is plotted as the relative axial distance from the silicon wafer coated with fibronectin. Scale bar, 5 μm. (h) SAIM axial height measurements of adhesion proteins tagged with fluorescent proteins in MCF10As with and without TGFβ treatment. Paxillin is the only protein to significantly change axial position >10 nm, suggesting that the position of paxillin moves relative to that of the adhesion as a whole. (i) Quantification of paxillin-GFP axial position in MCF10As with and without TGFβ treatment. Paxillin in treated cells is located at a significantly higher axial nanoscale position (*$p < 0.05$; >10 cells). (j) Representative images of the axial position of paxillin-mEmerald (N-terminal) in focal adhesions in PyMT and Met1 cells. Scale bar, 5 μm.

In sum, these data indicate that tumor MECs with an elevated propensity to metastasize (here, Met1) exert higher traction forces than less metastatic but malignant MECs (here, PyMT), due primarily to an increase in adhesion size, but also to an increase in the average force per integrin. This phenotype is shared by MECs that have undergone a TGFβ-induced EMT and should therefore also be recapitulated in the basal-like tumor MECs encountering a stiffened ECM (Figure 1, e–g). Indeed, when considered with the behavior of MECs invading into 3D, stiffened, confined ECMs or within microchannels (Figures 1 and 2), these findings suggest that tumor MECs that assemble larger adhesions and exert higher integrin-generated forces may be able to migrate more efficiently in confined microenvironments.

The integrin adhesions in cells with a basal-like phenotype are more stable and elongated

To clarify the molecular origins of the increased force per integrin within adhesions, we examined the organization and stability of the adhesions in epithelial MCF10AT MECs and compared our findings to those measured in MECs that had been induced to undergo an EMT by TGFβ treatment. We conducted live-cell imaging of focal adhesion dynamics using paxillin-mEmerald as a proxy adhesion marker in live cells (Figure 7a). Consistent with our traction force data and the model predictions, we noted that the stability of the integrin adhesions was increased in the TGFβ-treated MCF10AT MECs, as evidenced by slower adhesion turnover (Figure 7b). To explore whether differences in adhesion lifetime reflected an altered adhesion microstructure, we performed superresolution microscopy on cellular paxillin–enhanced green fluorescent protein (eGFP) using Bayesian analysis of bleaching and blinking (3B), which uses the fluctuations in the fluorophore intensities to infer molecular localization at subpixel resolutions (Cox *et al.*, 2011). Whereas adhesions in MCF10AT MECs were roughly circular in aspect, the adhesions assembled in TGFβ-treated MCF10AT MECs were elongated and featured well-developed linear structures (possibly templated by actin bundles; Figure 7, c and d), similar to the adhesions

observed in fibroblasts and other mesenchymal cells (Morimatsu *et al.*, 2015).

Alterations in adhesion stability and structure plausibly reflect differences in molecular composition (Zamir *et al.*, 1999; Yoshigi *et al.*, 2005; Wolfenson *et al.*, 2013). To investigate this possibility, we assayed the colocalization of tensin, a marker for fibrillar adhesions, with paxillin in MCF10AT MECs with and without TGFβ treatment (Figure 7e). Pearson's correlation coefficient between paxillin and tensin was significantly higher for the TGFβ-treated MECs, suggesting that the differences in integrin adhesion size and shape were mirrored by changes in molecular composition (Figure 7f). To further probe potential differences in molecular architecture, we performed scanning angle interference microscopy (SAIM; Paszek *et al.*, 2012; DuFort and Paszek, 2014) to measure the axial position of known adhesion proteins (Figure 7, g–i). We found that focal adhesion kinase (FAK), talin, vinculin, and zyxin retained the same relative axial positions in both MCF10A and TGFβ-treated MCF10As (referenced to the coverslip; Figure 7 h). Intriguingly, the position of paxillin relative to the silicon wafer substrate increased from an average of ~50 nm in the epithelial MCF10As to ~65 nm in the TGFβ-treated, EMT-induced MCF10As (Figure 7i). SAIM imaging revealed a similar qualitative shift in paxillin height between the epithelial PyMT tumor MECs and their TGFβ-treated EMT-induced counterparts (Figure 7j). Of importance, paxillin phosphorylation alone could not account for the shift in molecular height observed after EMT induction, as revealed by studies in which a nonphosphorylatable paxillin (mutated at tyrosine residues 31 and 118 to phenylalanine; paxillin$^{Y31/118F}$) localized at the same height as a wild-type paxillin in paxillin-null mouse fibroblasts transfected with equal quantities of transgene (Supplemental Figure S6). These findings suggest that MECs that recapitulate a basal-like phenotype or that underwent a mesenchymal transition not only exert more cellular–ECM integrin traction forces, but also assemble integrin adhesions that may be more stable and acquire a distinct cellular and subcellular organization.

Proteomics identifies a protein complex implicated in tumor cell invasion and metastasis recruited to integrin adhesions in cells with a basal-like phenotype

We next sought to determine whether the differences in integrin adhesion force, stability, and cellular and subcellular organization observed in the cells with a basal-like phenotype translated into distinct differences in molecular composition. Given the significant height changes we observed in paxillin in the EMT-induced MECs, we used a mass spectroscopic proteomics approach termed Bio-ID (Roux *et al.*, 2012) to explore whether this was reflected by altered molecular interactions. We fused a promiscuous biotin ligase protein (BirA*) to the N-terminus of paxillin-eGFP and expressed this construct in MCF10A MECs treated with vehicle or TGFβ to induce an EMT (Figure 8a; Dong *et al.*, 2016). Analogous measurements used BirA* fused to eGFP as a control for nonspecific biotinylation. Focusing on the consensus list of integrin adhesome proteins (Horton *et al.*, 2015; Figure 8b), we found that particularly interesting new cysteine-histidine-rich protein (PINCH; gene name LIMS1) was the most significantly enriched associated protein proximal to paxillin in the TGFβ-treated MCF10A MECs (highly abundant in TGFβ-treated cells and not present in untreated cells). Intensity correlation analysis of immunostained human MCF10A MECs showed that the amount of PINCH in paxillin-rich adhesions increased significantly in MCF10A MECs after TGFβ treatment (Supplemental Figure S7). Indeed, even in the epithelial MCF10A MECs that assembled sizeable integrin adhesions, PINCH was largely absent or diffusely colocalized. PINCH forms a complex with integrin-linked kinase (ILK) and α-parvin and interacts with paxillin at focal adhesions (Legate *et al.*, 2006), and knockout of PINCH suppresses migration and vinculin localization to adhesions (Gonzalez-Nieves *et al.*, 2013). Consistent with observations that ILK modulates breast tumor aggression and metastasis in vivo and has been linked to an EMT phenotype (White *et al.*, 2001; Persad and Dedhar, 2003; Hannigan *et al.*, 2005), we observed ILK enrichment at paxillin adhesions in MCF10A MECs that had been induced to undergo EMT by TGFβ treatment (Figure 8d). Immunostaining also revealed ILK localized to the paxillin adhesions in the PyMT tumor MECs after TGFβ treatment and in the PyMT tumor MECs interacting with a stiff ECM compared with those plated on a soft ECM (Figure 8, e and f). Of importance, immunoblot analysis showed that overall levels of total paxillin and phosphorylated paxillin, as well as of ILK, remained largely unchanged after TGFβ treatment (Supplemental Figure S8a). Thus the enhanced association of ILK proximal to paxillin in adhesions in TGFβ-treated cells was not the result of increased ILK expression. Further, abrogating myosin-related contractility reduced the association of ILK to paxillin-rich adhesions, indicating that the enhanced molecular interactions to paxillin were favored under conditions of elevated actomyosin-generated force (Supplemental Figure S8, b and c; Schiller *et al.*, 2013). These findings imply that the more prominent, longer-lasting integrin adhesions fostered by the elevated traction force in the metastatic and basal-like MECs facilitated the recruitment of a suite of paxillin-associated proteins that fosters tumor cell invasion within a dense and stiffened ECM.

Phosphorylation of paxillin by Src family kinases is elevated in the mammary tumor cells with a basal-like phenotype and enhances invasion within a stiff 3D ECM

Tumor cell invasion requires integrin adhesion turnover stimulated by the phosphorylation of key adhesion plaque proteins, including paxillin (Tumbarello *et al.*, 2005). Immunofluorescence analysis revealed that phosphorylation of paxillin (tyrosine 31) was elevated in the TGFβ-treated MCF10A MECs (Figure 9a). Paxillin tyrosine 31 and 118 phosphorylation was also enhanced in the PyMT MECs induced to undergo EMT by TGFβ treatment and in the invasive Met1 tumor MECs (Figure 9b and Supplemental Figure S9). We also detected strong phosphopaxillin staining at paxillin adhesions in basal-like leader PyMT tumor MECs invading into the 3D collagen/fibronectin gels in response to ECM stiffening (Figure 9c). Critically, preventing paxillin phosphorylation through ectopic expression of a nonphosphorylatable paxillin mutated at tyrosine residues 31 and 118 to phenylalanine (paxillin$^{Y31/118F}$) to hinder adhesion turnover (Webb *et al.*, 2004; Pasapera *et al.*, 2010; Plotnikov *et al.*, 2012) inhibited Met1 tumor cell invasion into a 3D stiffened collagen gel (Figure 9, d, and quantified in e). Paxillin phosphorylation is mediated predominantly by Src family kinases (Schaller, 2001), and our Bio-ID assay revealed that GIT2, a Src substrate, was enriched proximal to paxillin in TGFβ-treated MCF10A MECs (enrichment factor, ~4; Yu *et al.*, 2009, 2010; Bianchi-Smiraglia *et al.*, 2013; Figure 8b). We therefore examined whether Src activity was critical for the elevated paxillin phosphorylation and enhanced invasive phenotype of the Met1 MECs in response to a stiffened 3D collagen/fibronectin in the bioreactor. Consistently, treatment of the metastatic Met1 and PyMT multicellular spheroids with the Abl/Src inhibitor dasatinib (20 nM) reduced paxillin phosphorylation and significantly decreased invasion of the tumor cell within the stiffened collagen/fibronectin hydrogel (Figure 9f).

The clinical relevance of these findings was investigated by analysis of the Cancer Genome Atlas (TCGA) data set and patient

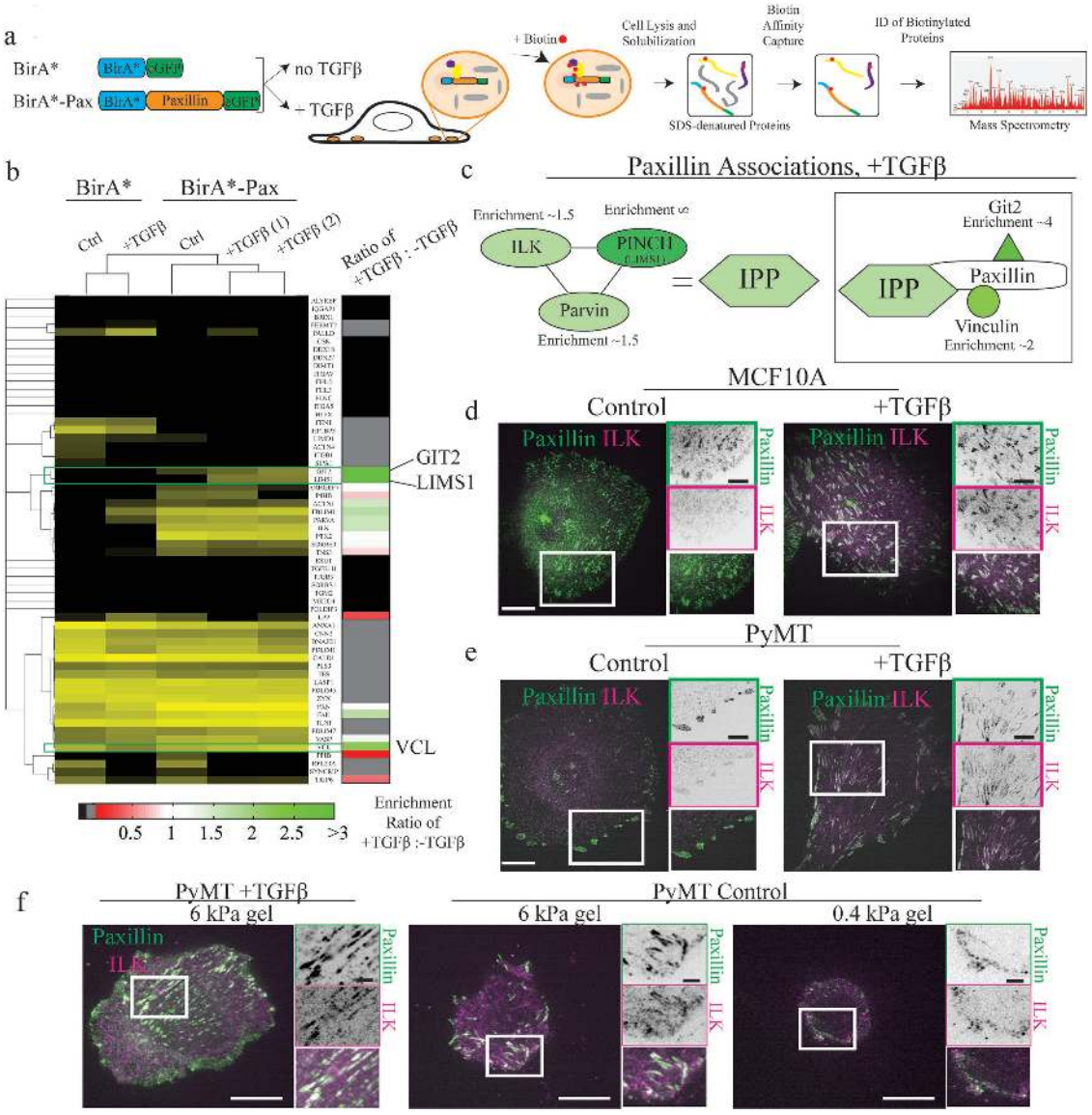

FIGURE 8: Proteomics identifies unique proteins recruited to paxillin in the integrin adhesions during EMT. (a) BioID technique. A control BirA*-eGFP construct and a BirA*-paxillin-eGFP construct are stably expressed in MCF10A cells, which are then treated with TGFβ to induce EMT. BirA*-paxillin-GFP localizes to FAs and biotinylates proteins adjacent to paxillin when biotin is added to the medium. Biotinylated proteins are isolated and identified by mass spectrometry. (b) Normalized spectral counts for the consensus adhesome were clustered on the basis of an uncentered Pearson correlation using Cluster 3.0 and visualized using Java TreeView. From a subgroup of known paxillin interactors, we identify GIT2, LIMS1 (PINCH), and vinculin as enriched in TGFβ-treated cells. Black indicates no protein detected in the +TGFβ:–TGFβ scale bar, and gray indicates no enrichment relative to the control. (c) Model for potential paxillin associations altered in response to TGFβ treatment. PINCH, GIT2, and vinculin localize adjacent to paxillin, and these associations are enriched in TGFβ-treated cells. (d–f) Immunofluorescence images of paxillin (green) and ILK (magenta). ILK is enriched in paxillin-rich adhesions in (d) MCF10A cells treated with TGFβ and (e) PyMT cells treated with TGFβ. Scale bar, 10 μm (main image), 5 μm (inset). (f) Immunofluorescence images of paxillin and ILK in PyMT cells on stiff (6 kPa) and soft (0.4 kPa) PA gels coated with fibronectin, showing that stiffness and TGFβ treatment modulate the recruitment of ILK to paxillin-rich plaques. Scale bar, 10 μm (main image), 2 μm (inset).

survival (Győrffy *et al.*, 2013). Gene expression data analysis revealed that patients with invasive breast cancer stratified into those with lymph node–positive cancers that had high levels of paxillin transcript also had a significantly worse chance of survival ($p < 0.001$; hazard ratio of 1.46 at 10 yr vs. patients with low paxillin levels; Figure 9g). Examination of the mortality hazard ratio for breast cancer patients with high gene expression of other integrin adhesion proteins also showed that patients with high FAK expression had a significantly higher risk of death ($p < 0.02$; hazard ratio, 1.34), whereas high expression of β1 integrin or talin did not associate with increased patient mortality (Supplemental Figure S10). Intriguingly, Src regulates FAK activity, FAK regulates integrin adhesion turnover, and FAK critically regulates cancer progression and metastasis (Deramaudt *et al.*, 2014; Sulzmaier *et al.*, 2014). Evaluation of reverse-phase protein array data derived from 892 human breast cancer patients further indicated that patients with

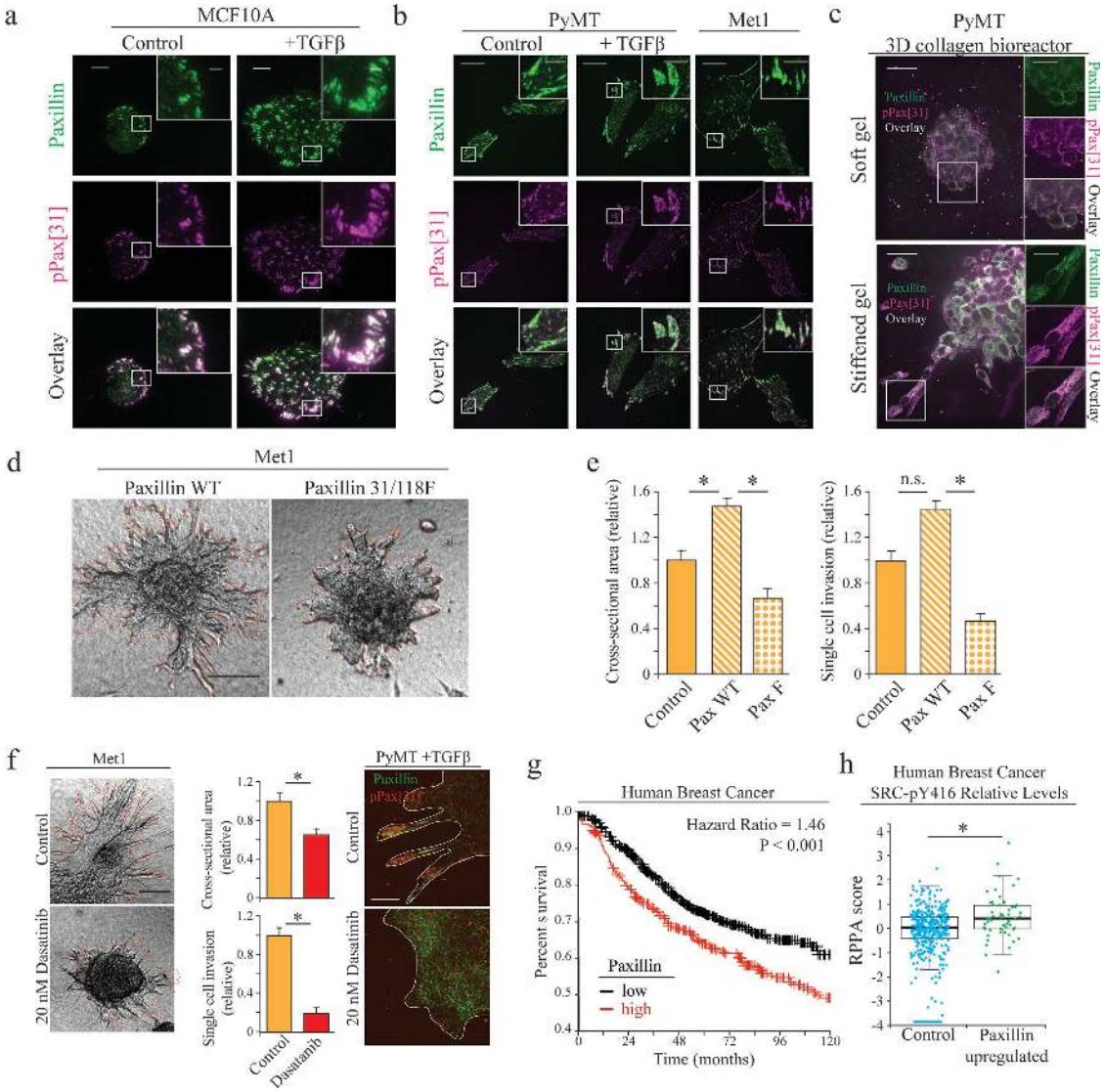

FIGURE 9: Enhanced paxillin phosphorylation permits invasion in cells with a basal phenotype. (a) Paxillin localization to the basal surface in MCF10A cells with and without TGFβ treatment visualized with immunofluorescence staining and TIRF imaging of paxillin and phosphorylated paxillin, pPax[31]. Scale bar, 10 μm (main image), 1 μm (inset). (b) Paxillin expression in PyMT, Met1, and PyMT + TGFβ visualized with immunofluorescence staining and confocal imaging of paxillin and phosphorylated paxillin pPax[31]. Scale bar, 10 μm (main image), 1 μm (inset). (c) Paxillin expression of PyMT cell spheroids visualized in soft and stiffened 3D collagen gel. Leader cells in stiffened gel have higher levels of phosphorylated paxillin indicated by pPax[31] immunostaining. Scale bar, 20 μm (main image), 10 μm (inset). (d) A 3D collagen invasion assay of multicellular spheroids composed of Met1 cells overexpressing either paxillin^{WT} or paxillin$^{Y31/118F}$ in 2.5 mg/ml 3D collagen gels for 72 h. Scale bar, 100 μm. (e) Quantification of invasion. Paxillin^{WT} overexpression significantly increased invasion compared with control or paxillin$^{Y31/118F}$ overexpression, as determined by cross-sectional area of spheroid and protrusions and single-cell invasion (*$p < 0.05$; >20 spheroids). (f) A 3D collagen invasion assay of multicellular spheroids composed of metastatic Met1 cells treated with dimethyl sulfoxide or 20 nM dasatinib, a Src/Abl inhibitor, in 2.5 mg/ml 3D collagen gels for 72 h. Dasatinib addition significantly decreased cell invasion, as determined by cross-sectional area and single-cell invasion (*$p < 0.05$; >15 spheroids). Scale bar, 100 μm. Dasatinib addition decreased levels of paxillin phosphorylation visualized by pPax[31] immunofluorescence. Scale bar, 5 μm. (g) Kaplan–Meier survival curve of invasive breast cancer patients expressing either high or low levels of paxillin. High paxillin levels are associated with a significantly worse chance of survival ($p < 0.001$; hazard ratio 1.46 at 10 yr). (h) Src phosphorylation levels via RPPA in TCGA breast cancer patients separated into control and paxillin–up-regulated groups. Paxillin up-regulation is correlated with a significant increase in Src phosphorylation at tyrosine 416 (*$p < 0.05$; >4200 patients).

elevated levels of paxillin also had significantly higher levels of phosphorylated Src-416, likely reflecting increased Src activity (Figure 9h). Thus the clinical data suggest that elevated total and Src family kinase-dependent phosphorylated paxillin may constitute tractable prognostic markers for decreased survival of patients with breast cancer. The cell biology studies imply that Src family kinase-dependent phosphorylation of paxillin may detect tumor cells with an intrinsic or tension-induced basal-like phenotype.

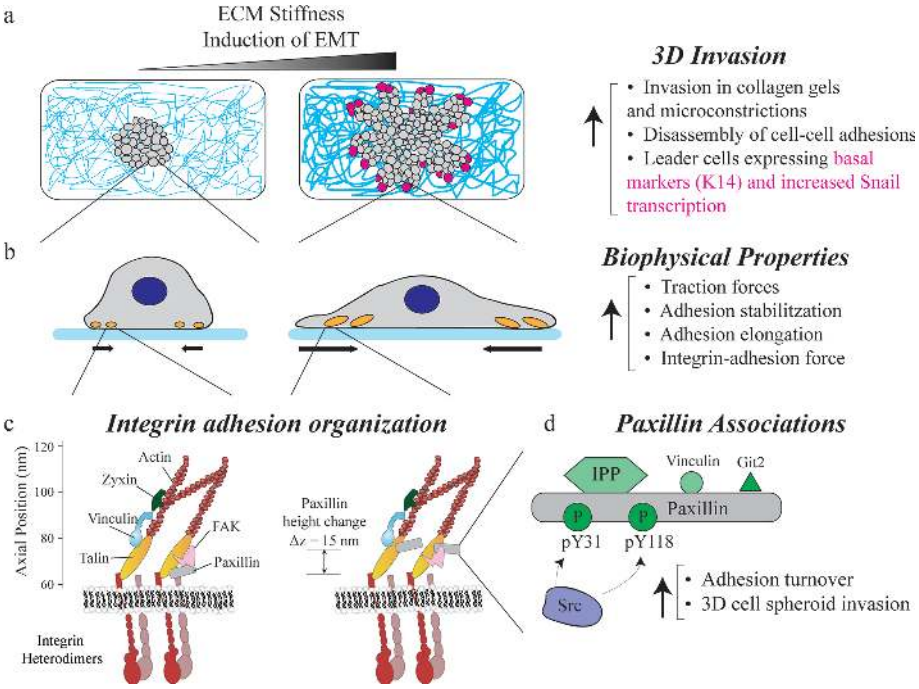

FIGURE 10: Mechanistic model. (a) ECM stiffness and induction of EMT enhance metastatic behavior, evidenced by increased invasion in 3D collagen matrices, expression of basal epithelial markers and Snail transcription in leader cells, and a higher propensity to migrate through small constrictions. (b) Adoption of a mesenchymal phenotype results in biophysical properties similar to those of basal-like cells, including higher integrin-mediated traction forces and more stable, elongated focal adhesions. (c) Axially scaled model of adhesion architecture changes in basal-like cells (TGFβ treated), showing the average increase in paxillin height of 15 nm. (d) EMT promotes the association of the ILK-PINCH-parvin (IPP) complex, vinculin, and Git2 directly to or in the vicinity of paxillin. Paxillin phosphorylation, mediated through kinases such as Src, regulate adhesion turnover and cell invasion.

DISCUSSION

In this study, we sought to understand the key cellular biophysical properties that endow breast tumor cells with a propensity to metastasize and in particular the ability to invade and migrate through confined spaces. We present evidence of underlying similarities between metastatic breast tumor cells, EMT-induced breast tumor cells, and breast tumor cells interacting with a stiffened ECM that exhibit a basal-like phenotype. In each of these cases, we found that the breast tumor cells assembled large, elongated, "mesenchymal-like" focal adhesions that exerted markedly higher forces than those assembled in analogous cells lines that were predominantly epithelial and less metastatic in nature. Our findings revealed that these intrinsic or microenvironment-induced differences in adhesion size and force output reflected alterations in adhesion architecture, turnover, and molecular composition. Of note, in each of these conditions, the paxillin adhesions in the invasive basal-like tumor cells associated with the recruitment of a suite of adhesion plaque proteins, including PINCH and ILK—components of the PINCH/parvin/ILK complex previously implicated in tumor cell invasion and metastasis (Persad and Dedhar, 2003; Legate *et al.*, 2006). In each of the invasive, basal-like cells, the paxillin that was recruited to focal adhesions was highly phosphorylated, a finding that is consistent with the notion that integrin adhesion turnover is essential for tumor cell invasion (Deramaudt *et al.*, 2014). Consistently, when the invasive breast tumor cells were treated with a broad-spectrum Src family kinase inhibitor that is currently used in the clinic to treat cancer, paxillin phosphorylation was reduced at focal adhesions, and the invasiveness of the metastatic breast tumor cells into a 3D stiff ECM was markedly decreased. Accordingly, our findings suggest that metastasis would be favored by tumor cells that either adopt or temporarily borrow a conserved, "EMT-like" or "basal-like" integrin adhesion phenotype with higher integrin-mediated traction force generation (Figure 10).

EMT has been proposed as a central, and even required, process in cancer metastasis (Chaffer and Weinberg, 2011; Tsai *et al.*, 2012). Cells in epithelial tissues are polarized, nonmigratory, and linked by mechanically robust intercellular adhesion complexes (Przybyla *et al.*, 2016). An EMT offers a conceptually attractive mechanism by which carcinoma cells could reverse these defining characteristics in order to migrate through surrounding tissues and establish distant metastases. Furthermore, invading malignant cells often exhibit at least some of the molecular hallmarks of EMT—for example, the expression and engagement of transcription factors such as Twist or Snail, which are considered defining features of EMT in a developmental context (Yilmaz and Christofori, 2009; Przybyla *et al.*, 2016). However, recent work has challenged the centrality of EMT to malignancy. In mouse models, distant metastases preferentially formed from multicellular aggregates rather than single cells. Further, metastasizing cells remained linked by robust cell–cell adhesions and maintained expression of E-cadherin, whose loss is classically considered a hallmark of EMT (Cheung *et al.*, 2013, 2016). In addition, cells invading into a 3D ECM from murine mammary tumor colonies, as well as human tumor colonies isolated from women with aggressive breast tumors, did not undergo a canonical EMT; instead, the leader cells adopted key features of a "basal-like" response while maintaining their epithelial phenotype (Nguyen-Ngoc *et al.*, 2012; Cheung and Ewald, 2014). More broadly, mesenchymal cells—for example, fibroblasts—are not intrinsically tumorigenic, and in humans are less likely to become cancerous than cells from epithelial tissues (Quail and Joyce, 2013). Our findings are consistent with these observations and imply that tumors cells may merely temporarily or permanently exploit basal-like features to facilitate their metastasis.

In the context of breast cancer, the perspective that a tumor need not undergo a complete EMT to metastasize has led to a revised model in which malignant epithelial cells adopt key features of basal-like/partial EMT cells and whose phenotypic characteristics may facilitate multicellular invasion into the surrounding tissue. Our data showed that an ECM with a stiffness matching that of the breast cancer stroma induced the leader PyMT epithelial cells within a tumor colony to adopt characteristics consistent with the "basal-like/partial EMT" phenotype, including cytokeratin 14 and Snail expression and partial disassembly of cell–cell adhesions, that was associated with their invasion into the surrounding matrix as loose cellular aggregates extending from the primary colony. The findings illustrate how the tissue microenvironment can promote the adoption of a presumably transient "basal-like" program that fosters tumor cell dissemination without compromising the overall epithelial

phenotype (Cheung *et al.*, 2013; Pickup *et al.*, 2013). Our studies thus provide a plausible explanation for the seemingly irreconcilable multicellular versus EMT phenotype as metastatic promoters. Critically, our observations suggest that malignant cells can either permanently or transiently borrow critical elements of a mesenchymal phenotype, notably the ability to exert large tractions on their surrounding ECM that would facilitate their dissemination through confined spaces. Our findings also predict that tumor cells should be able to adopt this metastatic adhesion phenotype without surrendering essential elements of their epithelial phenotype, such as cell–cell adhesion, which we and others showed can enhance survival in response to chemotherapy and during metastasis and would favor their ability to form macroscopic tumors (Weaver *et al.*, 2002; Loessner *et al.*, 2010; Longati *et al.*, 2013).

Metastatic cells that penetrate through confined spaces experience extensive cell deformation (Doyle *et al.*, 2013; Wolf *et al.*, 2013). In some studies, biophysical measurements revealed that metastatic tumor cells have a lower effective stiffness than their primary tumor counterparts (Darling *et al.*, 2007; Swaminathan *et al.*, 2011). A decrease in cell stiffness, believed to be linked to induction of an EMT, presumably provides the metastatic cell with a means to migrate through confined spaces (Osborne *et al.*, 2014; McGrail *et al.*, 2015). In our hands, the prometastatic Met1 and EMT-induced PyMT MECs exhibited an enhanced ability to pass through confined channels relative to the less metastatic parental PyMT MECs. However, AFM indentation revealed that this enhanced migratory ability did not consistently correlate with an increase in cortical deformability. However, we recognize that the AFM indentation measurements performed in the present studies report cell cortical stiffness, whereas the overall elasticity of the cytoskeleton may differ significantly. Another important proviso is that alterations in nuclear deformability, as we showed, also change after TGFβ treatment–induced EMT, and this elevated compliance may itself significantly contribute to the cells' ability to navigate through constrictions. Nevertheless, our findings do suggest that an increase in cytoskeletal compliance is not an absolute prerequisite for cell migration through a confined microenvironment (Pathak and Kumar, 2012; Charras and Sahai, 2014; Lautscham *et al.*, 2015). Instead, our studies suggest that an obvious likely contributor to the ability of cells to pass through constrictions is the ability of the disseminating cells to generate substantial tractions at their ECM adhesions. In short, our observations are consistent with the idea that cells that have a higher propensity to metastasize are more contractile, and yet their nucleus is more deformable. Thus cell contractility and stiffness are not synonymous, particularly in a diseased state in which cells adopt different phenotypes and/or behaviors than during normal physiological function.

More broadly, generation of integrin–ECM traction by cancer cells is linked to matrix stiffening and matrix remodeling (Paszek *et al.*, 2005; Schedin and Keely, 2011; Jansen *et al.*, 2013; Rubashkin *et al.*, 2014a), both of which are believed to contribute to metastasis (Lu *et al.*, 2012; Pickup *et al.*, 2014). Consistently, prior studies correlated increased traction stresses with metastatic potential, albeit using a variety of cancer cell types with diverse origins that may or may not reflect a true acquisition of a metastatic phenotype (Kraning-Rush *et al.*, 2012). Here we found that the Met1 MECs and EMT-induced PyMT MECs increased their traction forces relative to the parental PyMT MECs, findings that are consistent with results reported here and elsewhere showing that a stiff ECM increases cellular traction force and fosters tumor cell metastasis (Paszek *et al.*, 2005; Kraning-Rush *et al.*, 2012; Pickup *et al.*, 2013). Of interest, an increase in cellular traction force is required for endoderm specification and is proposed to guide osteogenesis and myogenesis (Lee *et al.*, 2015; Taylor- Weiner *et al.*, 2015). Our data are thus consistent with the general idea that increased traction forces exhibited by prometastatic cancer cells may reflect a selective hijacking of one critical aspect of the EMT phenotype.

We present a simple physical model, modified from previous iterations (Chan and Odde, 2008; Bangasser *et al.*, 2013; Elosegui-Artola *et al.*, 2016), that could explain the cell-level changes in adhesion and contractility that facilitate metastasis. A principal prediction arising from this model is that both enhanced cell ECM adhesion (an increased number of "clutches") and increased contractility (an increased number of "motors") are required for the increase in cellular traction that accompanies the malignant phenotype. Our experimental measurements of cellular ECM traction and adhesion size, architecture, and dynamics are consistent with this general prediction. In particular, our MTS measurements indicated large increases in cellular traction forces in all of the breast tumor cell lines with a prometastatic or an EMT-like phenotype and revealed that the forces were likely transmitted through larger force-producing integrin adhesions. Intriguingly, our data revealed that the average force per integrin complex was modestly increased, suggesting that, in addition to an increase in clutch number, individual bond properties were also altered by addition of TGFβ. For example, the increased force per bond could be due to a modest increase in the characteristic bond force (F_{bond}) or modest decrease in basal clutch unbinding rate (k_{off}). Higher forces at the single-integrin level may plausibly reflect force-mediated "outside-in" signaling to drive clutch and motor addition (as in our biophysical model), which would then link to integrin-dependent intracellular signaling to drive actomyosin-dependent cytoskeletal tension. In the case of metastatic tumors, which exhibit increased integrin-linked forces and elevated "oncogene-dependent" actomyosin contractility, this relationship is predicted to reset the state of cellular tensional homeostasis to a higher level (Paszek and Weaver, 2004; Laklai *et al.*, 2016).

Our data suggest that differences in adhesion properties reflect changes in adhesion molecular composition. We found that the large, force-producing adhesions assembled in the MECs that had undergone an EMT recruited more PINCH and ILK, which comprise part of the PINCH/Parvin/ILK complex, which has been strongly implicated in tumor cell invasion and metastasis (Persad and Dedhar, 2003; Legate *et al.*, 2006). Our findings are also consistent with cell studies implicating ILK in an EMT and transgenic mouse work showing that ILK overexpression promotes breast tumor progression, whereas its knockdown reduces tumor aggression (White *et al.*, 2001; Hannigan *et al.*, 2005; Serrano *et al.*, 2012; Pang *et al.*, 2016). Thus adoption of the EMT-like adhesion phenotype by tumor cells may favor the recruitment of key signaling molecules that facilitate tumor cell invasion. Consistently, we found that paxillin displayed a pronounced shift in *z* height relative to the membrane in cells that had gone an EMT, suggestive of a differential role in epithelial versus mesenchymal cells.

Adhesion turnover is required for cell migration and for the metastatic dissemination of malignant cells (Friedl and Alexander, 2011). Consistent with this concept, despite the fact that the mammary tumor cells that had undergone an EMT assembled large, distinct focal adhesions and recruited a large repertoire of adhesion plaque proteins, they were also highly dynamic. The integrin adhesions formed by the metastatic breast tumor cells, breast tumor cells induced to undergo an EMT, and the basal-like PyMT tumor colonies interacting with a stiffened ECM also had elevated levels of phosphorylated paxillin, an observation echoing prior reports that paxillin phosphorylation is higher in metastatic cells and

in cells treated with TGFβ (Tumbarello *et al.*, 2005). Phosphorylation of paxillin by Src family kinases acts to induce both adhesion growth and disassembly and hence serves as a master regulator of adhesion stability (Turner, 2000; Webb *et al.*, 2004; Zaidel-Bar *et al.*, 2006; Wolfenson *et al.*, 2011). We found that tumor cells interacting with a stiffened 3D ECM also exhibited higher levels of phosphorylated paxillin at their integrin adhesions, which may reflect an adaptation of the cells' inherent sensing response to a soft substrate (Plotnikov *et al.*, 2012). Regardless, we showed that blocking paxillin phosphorylation either by point mutagenesis or by adding a small-molecule inhibitor of a Src family kinase used in the clinic blocked the 3D invasion of Met1 MECs. Moreover, epidemiological data indicate that high paxillin expression correlates with decreased patient survival, and phospho-array data show that elevated tumor paxillin associates with high Src kinase levels and activity. Thus alterations in adhesion structure and dynamics may be directly linked to patient outcome, and assessment of integrin adhesion composition may constitute an untapped prognostic indicator.

MATERIALS AND METHODS

Cell culture and reagents

MECs, including nonmalignant MCF10A (American Type Culture Collection; verified by epithelial cellular morphology in two dimensions, ability to form hollow, polarized acini in 3D rBM gels, and expression of epithelial markers, including E-cadherin and cytokeratins 8 and 14) and premalignant Ha-Ras–transformed MCF10AT (Karmanos Cancer Institute; verified by epithelial cell morphology in two dimensions) were cultured as described (Rubashkin *et al.*, 2014a). Tumorigenic MEC lines PyMT Flox3 and metastatic Met1 (kind gift of the Moses laboratory, Vanderbilt University) were cultured as described previously (Borowsky *et al.*, 2005).

The 3D multicellular spheroids were generated in rBM (Matrigel; Corning) suspension cultures as described (Rubashkin *et al.*, 2014a). MCF10A and Met1 MECs were flow sorted on a FACSAria II cell sorter (BD Biosciences) via primary and secondary antibody staining for top ~20% or bottom ~20% expression of α_5 integrin, β_1 integrin, or $\alpha_v\beta_3$ integrin. The chemokine human TGFβ at 10 nM (PeproTech or Sigma-Aldrich) was used for 3 d to induce mesenchymal behavior. The small-molecule inhibitor dasatinib was used at 20 nM (Cayman Chemical).

Expression constructs

Transient plasmid constructs included Clontech vectors containing N- and C-terminus–tagged vinculin-mEmerald, paxillin-mCherry, paxillin-mEmerald, farnesyl-mEmerald, farnesyl-mCherry, FAK-mEmerald, Talin-mEmerald, Talin-mCherry, Zyxin-mEmerald, Tensin-mEmerald, and Tensin-mCherry. Expression constructs were provided by the Davidson Lab. Piggybac transposable plasmids containing eGFP-paxillin and eGFP-paxillin$^{Y31/118F}$ were synthesized and cloned (Epoch Life Science, Sugar Land, TX) into *Bsa*I-digested pHULK piggyBac Mammalian Expression Vector–CometGFP (DNA 2.0).

Stable cell lines inducibly expressing BirA*-paxillin derivatives were prepared using a custom-built PiggyBac transposable vector, pPB puro Tet. Briefly, pPB puro Tet includes the hepatamerized tetracycline (tet) operator minimal CMV promoter, which drives expression of a transgene with a 5′ chimeric intron and polyadenylation signal derived from bovine growth hormone. pPB puro Tet also includes an expression cassette for puromycin selection in reverse orientation. BirA* (Roux *et al.*, 2012) was modified with three tandem repeats of the myc 9E10 epitope at the N-terminus and a 22–amino acid, C-terminal glycine- and serine-rich flexible linker (N22). The modified BirA* was then cloned in-frame with full-length paxillin-eGFP (Addgene plasmid 15233) at the N-terminus, such that the final construct had 3xmyc-BirA*-N22-paxillin-eGFP in order from N- to C-terminus. A fusion of mEmerald to the C-terminus of myc-tagged BirA* served as a control.

Transient transfection was performed using either Lipofectamine 2000 reagent or the Lonza Nucleofector Kit V, with program T024 for all epithelial cell lines and U024 for other cell lines. Recombinant lentivirus of the tet-promoter rtTA (neo) was prepared by transient transfection into HEK-293T cells, generating lentivirus titer used to transduce cells, as previously described (Rubashkin *et al.*, 2014a). Target cells constitutively expressing the synthetic reverse Tet transcriptional transactivator rtTAs-M2 were prepared by transduction with a G418 selectable lentiviral vector. These cells were transiently transfected with pPB puro Tet constructs and an expression construct for a hyperactive piggyBac transposase pCMV-HAhyPBase (generous gift of Allan Bradley, The Wellcome Trust Sanger Institute; Yusa *et al.*, 2011).

Stable cell lines were selected in 200 ng/ml G418, 380 ng/ml hygromycin, or 1 µg/ml puromycin and sorted on a FACSAria II cell sorter (BD Biosciences) for fluorescent protein expression. Expression of inducible protein-encoding gene was induced with 200 ng/ml doxycycline in growth medium for 1 d before experimentation.

Hydrogel and substrate preparation

Collagen gels were fabricated by diluting 2.5 mg/ml acid-solubilized rat tail collagen (BD) in 1:1 DMEM-F12 (Invitrogen), neutralizing to pH 7.4 with 1 M NaOH. For 3D collagen gels, a base layer of ~250-µm thickness was cast at 37°C for 30 min, followed by a second layer that included the cell suspension, which was also allowed to solidify over 30 min. Two-dimensional (2D) PA gels (height ~200 µm) were fabricated by varying the acrylamide and cross-linker concentration and assessing stiffness using either ATM or a shear rheometer (Johnson *et al.*, 2007). Red fluorescent beads (100 nm; Invitrogen) were incorporated in the PA gels at 1:300 dilution relative to the manufacturer's concentration and centrifuged at 200 RCF to move the beads to the top surface of the gels for TFM. PA gels were functionalized with 10 µg/ml human fibronectin (Millipore) as described (Lakins *et al.*, 2012).

N-type [100]-orientation silicon wafers with 1933-nm silicon oxide (1 cm x 1 cm; Addison Engineering) and borosilicate glass coverslips (~150 µm thick) were cleaned by successive sonication in acetone and 1 M KOH (20 min), followed by chemical activation with silane (0.5% (3-aminopropyl)trimethoxysilane)) and glutaraldehyde (0.5% in water). The substrates were then ultraviolet- and ethanol-sterilized and incubated overnight (4°C) in extracellular matrix (human fibronectin, 10 µg/ml; Millipore). Before use, substrates were washed in phosphate-buffered saline (PBS; five times; pH 7.4), treated with sodium borohydride (20 mg/ml), and washed with PBS. SAIM calibration wafers were prepared by sonicating carboxylate-modified red fluorescent spheres (100 nm; Invitrogen), following by bead deposition (5×10^8 beads/ml) in NaCl (100 mM) PBS solution as described (Paszek *et al.*, 2012).

Immunofluorescence

Cells were cultured on various substrates overnight and then fixed with 4% paraformaldehyde (PFA; 2D: 20 min, room temperature; 3D: overnight, 4°C) and stained as described (Levental *et al.*, 2009). Primary antibodies against paxillin (5H11, Millipore; 610620, BD; P1093, Sigma-Aldrich; 32084, Abcam), phospho–paxillin-tyrosine 118 (44-722G, Life Technologies; 2541, Cell Signaling), phospho–paxillin-tyrosine 31 (44-720F, Life Technologies), vinculin (hVIN-1,

Sigma-Aldrich; 700062, Invitrogen; V284, Santa Cruz Biotechnology), phospho–FAK-tyrosine 397 (44-625G, Invitrogen), vimentin (D21H3, Cell Signaling), β-catenin (8480, Cell Signaling), K14 (PRB-115P, Covance), K8+18 (20R-CP004, Fitzgerald Industries), PINCH (EP1944, Abcam), ILK (611803, BD), and Alexa Fluor–phalloidin (Invitrogen) were used. Secondary antibodies used include Alexa Fluor goat anti-mouse, anti-rabbit, and anti-rat (488, 568, and 633 conjugates). For ILK immunofluorescence (IF), cells were fixed in 100% ice-cold methanol.

Microscopy and analysis

Unless otherwise noted, SAIM, TFM, confocal, and spheroid invasion assay imaging were performed on motorized total internal reflection fluorescence (TIRF) inverted microscopes (Ti-E Perfect Focus System; Nikon) controlled by MetaMorph (Molecular Devices) and Nikon Elements software and equipped with 488-, 561-, and 640-nm lasers, 350/50 epifluorescence, a CSU-X1 spinning-disk confocal unit (Yokogawa Electric Company), electronic shutters, motorized stage, a scientific complementary metal-oxide-semiconductor (sCMOS) camera (Zyla 5.5 megapixel, Andor; or Orca Flash, Hamamatsu), and an electron-multiplying charge-coupled device (EMCCD) camera (QuantEM 512; Photometrics). Temperature and CO_2 were controlled by an environmental chamber and proportional integral derivative–controlled heater (In-Vivo Scientific). Samples were imaged with 100×/1.49 numerical aperture (NA) TIRF oil-immersion, 40×/1.2 NA long-working-distance water-immersion, 20×/0.75 NA air, and 10×/0.45 NA air objectives. For live-cell imaging, phenol red–free growth medium with 10 mM 4-(2-hydroxyethyl)-1-piperazineethanesulfonic acid (HEPES; pH 7.4) was used. For 3D imaging, confocal image slices were taken at 0.2- or 1.0-µm slices and the individual planes were maximum intensity *z*-projected for 2D visualization. Custom software packages for image analysis were written in Python, using ImageJ and the Eclipse Development Environment in Linux. Images were subject to a Gaussian blur of 1.0 pixel to smooth background noise. Intensity and colocalization measurements of single confocal planes were calculated on a pixel-by-pixel basis. Single-cell invasion, acini and cell protrusions, and cell adhesion length were quantified manually and verified qualitatively across three independent experiments. Acini cross-sectional area was quantified with the free-hand selection tool in ImageJ. Focal adhesion lifetimes were quantified manually and verified qualitatively across three independent experiments. SAIM was performed as described (Paszek *et al.*, 2012; Rubashkin *et al.*, 2014a), using data analysis and 3D visualization programs written in Matlab and Python using libraries distributed by Enthought.

Collagen invasion assays in 3D bioreactor

PyMT organoids were cultured in rBM (Corning) for 3–5 d. The organoids were isolated by solubilizing the gels using PBS-EDTA. The isolated organoids were subsequently embedded in 2.5 mg/ml collagen I solution supplemented with fibronectin (1 µg/ml) and rBM (1%). The collagen gels were stretched in a tension bioreactor with 0 or 10% strain for 72 h (Cassereau *et al.*, 2015). Organoids were fixed with 1% PFA overnight for subsequent IF staining. Snail-YFP knock-in reporter tumor cells were kindly provided by Robert Weinberg (Ye *et al.*, 2015). Tumor cells were cultured in rBM for 3–5 d and transferred to either untreated or ribose-stiffened collagen gels. After 48 h, organoids were fixed and stained for indicated proteins.

Microchannel migration assays

Migration experiments in microfluidic devices were carried out as described previously (Davidson *et al.*, 2014, 2015; Denais *et al.*, 2016). Briefly, the migration devices contain 5-µm-tall channels with constrictions ranging from 1 to 15 µm in width. Migration channels are flanked on either side by two unconfined regions with a height of 250 µm (Davidson *et al.*, 2015). Molds of the migration devices were generated using two-layered SU-8 photolithography as described previously (Davidson *et al.*, 2014). Replicas of the molds were made from a two-component Sylgard 184 polydimethylsiloxane (PDMS) kit (Dow Corning) using the (1:10) manufacturer's recipe and cured for 2 h at 65°C. After curing, devices were cut to size, and holes were punched for cell-seeding ports and media reservoirs. A plasma cleaner (Harrick Plasma) was used to covalently bind microfluidic devices to glass coverslips that had been soaked in 0.2 M HCl overnight, rinsed with water and isopropanol, and dried. To improve adhesion after plasma cleaning, the completed devices were heated on a hot plate at 95°C for 5 min before sterilization with 70% ethanol. Devices were rinsed and treated with 20 µg/ml fibronectin (Millipore) overnight at 4°C. After incubation, the devices were rinsed with 1× PBS and cell culture medium. For the experiments, 30,000 cells/device were loaded into each device and allowed to attach overnight. Experiments were conducted with a 0–10% fetal bovine serum (FBS) gradient across the constrictions to stimulate directed migration, with cell medium supplemented with 25 mM HEPES. Devices were sealed with a glass coverslip to minimize evaporation and placed on a temperature-controlled stage (37°C) of an inverted Zeiss Observer Z1 microscope equipped with a CCD camera (Photometrics CoolSNAP KINO) and a motorized stage. Images for time-lapse sequences were acquired every 10 min for at least 12 h through a 20× air objective (0.8 NA) using ZEN software (Zeiss).

Images were analyzed using ZEN and ImageJ. Cell transit times through constrictions were measured for individual cells based on time-lapse sequences, with the starting point defined by the frame showing the first signs of nuclear deformation as a cell entered into a constriction, and the ending point defined by the frame at which the cell had migrated through the constriction and the nucleus was no longer "pinched." The fraction of cells that had passed through the first row of constrictions was determined using the final frame of each time-lapse series (i.e., 36-h after cell seeding). We quantified the number of cells that were located beyond the first constriction and the total number of cells that entered the 5-µm-tall channels. All experimental results are based on at least three independent experiments. Statistical analysis of transit times was determined using a Kruskal–Wallis test with Dunn's multiple comparisons because the transit times did not follow a Gaussian distribution. Fisher's exact test was used to compare the fraction of cells that had passed the first constriction between different conditions. The SE of the cell fraction was calculated according to the equation describing the SE for a binomial distribution:

$$\mathrm{SE} = \sqrt{\left(\frac{p(1-p)}{n}\right)}$$

where p is the fraction of cells that passed through the first row of constrictions and n is the total number of cells. Statistical tests were performed in GraphPad Prism.

Atomic force microscopy

Cells were seeded on polyacrylamide gels with 2.7-kPa stiffness for 18 h. Hydrogels were then placed on the center of a standard microscopy slide and anchored using two-sided tape. Cells were kept hydrated in a droplet of HEPES-buffered medium (at room temperature) while force measurements were performed on an Asylum Research (Santa Barbara, CA) MFP-3D atomic force microscope.

All samples were measured in liquid in contact mode using Novascan 2.5-μm-radius beaded silica glass tip (k = 0.06 N/m) cantilevers, which were calibrated by the thermal tune method. Force measurements were collected at multiple points across the surface of the gels and cells at a maximum trigger force of 2.0 nN. The resulting force data were converted into elastic modulus using the Hertz Model program in IgorPro v6.22A. Measurements were also repeated with pointed-tipped Asylum Research TR400PB silicon nitride (k = 0.02 N/m) cantilevers, showing a similar trend. Surface plots were generated using the *surf()* function in Matlab. To determine cell elasticity, height cutoffs were chosen based on the height maps to assign pixel values associated with the cell versus the gel.

Micropipette aspiration

Micropipette aspiration through 3-μm-wide, 5-μm-high channels was performed using microfluidic devices fabricated as described in Denais *et al.* (2016). PDMS molds of the devices were filled with a 2% bovine serum albumin (BSA)/0.2% FBS solution. Cells were trypsinized and resuspended in the 2% BSA/0.2% FBS solution containing Hoechst 33342 for nuclear visualization. The cell suspension was perfused into the devices at constant pressure using a MCFS-EZ pressure controller (Fluigent). Channels were cleared by manual backflushing, and nuclear deformation of cells entering the channels was observed at 5 s intervals using a 20×/0.4 NA phase contrast objective and Hamamatsu ORCA Flash 4.0 V2 camera. Images were analyzed using a custom-written MATLAB algorithm.

Traction force microscopy

Cells were seeded overnight on PA gels with 100-nm fluorescent red beads. Images of cells and beads were taken at 20× before adding 0.01% SDS to lyse the cells from the surface. A second picture of the beads was taken afterward that was later aligned via the ImageJ (http://rsb.info.nih.gov/ij) registration plug-in StackReg. To assess bead movement, a particle image velocimetry (PIV) program was implemented in ImageJ as described previously (Tseng *et al.*, 2012). The iterative scheme included a first pass at 32/64 (i.e., interrogation and search window size in pixels), followed by a second pass at 16/32, all at a correlation threshold of 0.60. Cross-correlation PIV was used for traction measurements on gels of different stiffness, with three iterative schemes of 128, 64, and 32 as the interrogation window sizes. For PIV postprocessing, a normalized mean test (NMT) was performed as described (Tseng *et al.*, 2012) with NMT noise of 0.2 and threshold of 2.0 as starting parameters. Parameters were altered to correct for erroneous vectors. The traction force was calculated by the Fourier transform traction cytometry (FTTC) method with a Poisson ratio of 0.5. For measurements of the PyMT/Met1 and MCF10AT system, no regulation factor was used. To quantify the traction forces of MCF10A MECs on gels of different stiffness, we performed a regularization sweep to determine an optimal value and chose a constant of 10^{-10} for all of the conditions. Total and maximum traction forces were calculated using a mask of cell area from the bright-field image overlaid onto a per-pixel magnitude plot of the traction vectors. The PIV and FTTC microscopy software for ImageJ was kindly made available by Qingzong Tseng (https://sites.google.com/site/qingzongtseng/tfm).

Motor-clutch model of cell traction

Stochastic simulations of a motor-clutch model of cellular traction were modified from previous models (Chan and Odde, 2008; Bangasser *et al.*, 2013). The base model contains eight parameters that describe numbers and physical properties of myosin motors and molecular clutches (e.g., integrin-mediated adhesion complexes), as well as kinetic rates for binding and unbinding of molecular clutches. Monte Carlo simulations were executed using a Gillespie stochastic simulation algorithm (Gillespie, 1977) run on in-house simulation computers using Matlab (MathWorks, Natick, MA), version 2014b. For a detailed description of the simulation and relevant parameters, refer to the Supplemental Materials. The modified reinforcement model includes kinetic rates for addition of molecular clutches to the ensemble when a threshold force is reached by engaged clutches:

$$K_{\text{add}} = K_{\text{add,base}} \times n_{\text{clutch}}\left(F > F_{\text{threshold}}\right) \times \frac{n_{\text{clutch,max}} - n_{\text{clutch}}}{n_{\text{clutch,max}}}$$

where K_{add} is a basal first-order clutch addition rate constant, $F_{\text{threshold}}$ is a threshold force for clutch reinforcement signaling, and $n_{\text{clutch,max}}$ represents the total number of available clutches in the cell.

Cell areas in all simulations were approximated from simulation results by calculating the size of a disk-shaped cell from the length of an F-actin bundle. Actin filament assembly and cycling between G- and F-actin pools is calculated by an actin mass balance,

$$\left[\text{Actin}_{\text{total}}\right] = \left[\text{G-actin}\right] + \left[\text{F-actin}\right]$$

where [G-actin] and [F-actin] are relative lengths of actin assigned to a soluble pool and filaments, respectively. Leading-edge protrusion velocity ($v_{\text{protrusion}}$) scales with the amount of available actin ([G-actin]) and is opposed by actin retrograde flow (v_{filament}) to give the following relationship for cell spreading rate:

$$V_{\text{spread}} = V_{\text{protrusion}} - V_{\text{filament}}$$

Traction force outputs from simulations are in one-dimensional (1D) forces, whereas experimental measures of traction force result in 2D stresses on a compliant gel. To draw comparisons between simulation and experiment, we used a previously described approach to derive a relationship between 1D forces and 2D stresses on a continuous substrate (Ghibaudo *et al.*, 2008), as was previously described for stochastic simulations of cell traction (Elosegui-Artola *et al.*, 2014, 2016). Here P_{traction} is traction stress, and F_{traction} is traction force:

$$P_{\text{traction}} = \frac{F_{\text{traction}}}{\pi r_{\text{adhesion}}^2 \left(= 1\ \mu\text{m}^2\right)} \rightarrow P_{\text{traction}} = F_{\text{traction}}$$

A compliant substrate is modeled as an elastic spring with stiffness constant $\kappa_{\text{substrate}}$ and effective Young's modulus (E_{eff}) given by

$$E_{\text{eff}} = \frac{9 \times \kappa_{\text{substrate}}}{4\pi r_{\text{adhesion}}} \rightarrow E_{\text{eff}} \sim 1.3\ \kappa_{\text{substrate}}$$

Integrin force sensor measurements

The MTSs were adapted from sensors described previously (Morimatsu *et al.*, 2015), using cysteine-maleimide chemistry to attach the donor Alexa 546 dye and the acceptor Alexa 647 dye (Life Technologies). This modified MTS presents an RGD peptide derived from fibronectin TVYAVTG**RGD**SPASSAA. Perfusion chambers were attached to PEGylated coverslips as previously described (Morimatsu *et al.*, 2015). Briefly, labeled MTSs (~100 nM) were added to the flow cell and incubated for 30 min, followed by Pluronic F-127 (0.2% wt/vol) for ~1 min to prevent nonspecific cell attachment. All of these steps were preceded by a PBS wash to remove excess reagent from

the prior step. The cells were then added and incubated for at least 1 h at 37 °C before imaging.

Images were taken using TIRF microscopy on an inverted microscope (Nikon TiE) with an Apo TIRF 100× oil objective lens, NA 1.49 (Nikon). Data were acquired with a 200-ms exposure using either an EMCCD camera (Andor iXon) or an sCMOS camera (Hamamatsu Orca Flash). The no-load FRET efficiency and gamma factor (γ) were measured at the single-molecule level as described previously. To calculate FRET index ($FRET_i$), we divide the acceptor intensity, A (background subtracted), by the sum of the acceptor and donor (D) intensities (also background subtracted): $FRET_i = A/(A + D)$. Using the measured FRET index, we calculate the FRET efficiency (E), using the measured fraction of double-labeled sensor ($\alpha \approx 0.90$):

$$E = \frac{FRET_i}{\alpha\left(\gamma - FRET_i\gamma + FRET_i\right)}$$

We then convert from FRET efficiency, E, to an average force per sensor molecule at each pixel, using a previously measured calibration curve modified to incorporate the photophysical properties of the dyes used here (Morimatsu *et al.*, 2015).

A detailed explanation of calculations of the average force per sensor and total force per cell was given previously (Morimatsu *et al.*, 2015). Briefly, to measure the average force per sensor, we first segmented the images from the paxillin-eGFP signal or the FRET index signal. These images were normalized, boxcar averaged with a rotating reference frame, and then thresholded to create a binary mask. The binary mask was used for a watershed algorithm to isolate individual islands, which were then combined and indexed with custom-written MATLAB code with minimum adhesion size of 0.5 μm^2. The average force per sensor was calculated by converting the FRET efficiency values to force values of individual pixels within the segmented regions. The total force per cell was calculated using FRET images of the entire cell taken on a Hamamatsu sCMOS camera. The FRET values in the segmented pixels were then converted to force and summed over all of the adhesions in the entire cell.

3B superresolution analysis

The 3B algorithm uses a Bayesian analysis technique to determine the positions of fluorophores based on patterns of blinking and bleaching events (Cox *et al.*, 2011). Data were recorded on an EMCCD camera (Andor iXon) for ~200–300 frames at 20 frames/s. The images were then processed with the 3B algorithm on virtual machines hosted on Amazon's EC2 cloud computing service (Hu *et al.*, 2013). Each calculation ran on the compute-optimized c3.large servers for ~40 iterations. The positions and intensities of the fluorophores as determined by the 3B analysis were plotted on a coordinate system scaled by a factor of three, representing a threefold increase in effective resolution.

Proteomics experiment and analysis

The biotin ligase protocol was modified from the previously published method (Roux *et al.*, 2012), with some modifications outlined here. Four 10-cm dishes (~20 million cells) of MCF10A MECs stably expressing BirA* constructs were cultured on tissue culture plastic and treated with TGFβ for 3 d. The cells were then incubated in medium supplemented with 50 μM biotin (B4639; Sigma-Aldrich) for 24 h before lysate collection. Cells were detached using trypsin-EDTA, washed three times with cold DPBS, and resuspended in 1.6 ml of ice-cold RIPA buffer (50 mM Tris-HCl, pH 7.5, 150 mM NaCl, 1 mM EDTA, 1 mM ethylene glycol tetraacetic acid, 0.5% sodium deoxycholate, 0.1% SDS, 1% NP-40) with protease inhibitor cocktail (539134; Calbiochem). The lysates were incubated on ice for 1 h, followed by three sonication repeats using 10-s bursts at 30% amplitude and 30-s rest (Sonics VCX130). Supernatant was collected after 30-min centrifugation at 16,000 × *g* at 4 °C and incubated with 500 μl of DPBS-prewashed streptavidin Dynabeads (65001; ThermoFisher) overnight at 4 °C on an end-over-end mixer.

Dynabeads were collected the next day and washed for 5 min at room temperature twice with 1 ml of buffer 1 (2% SDS in H_2O), once with 1 ml of buffer 2 (0.1% sodium deoxycholate, 1% Triton X-100, 500 mM NaCl, 1 mM EDTA, 50 mM HEPES, pH 7.5), once with 1 ml of buffer 3 (250 mM LiCl, 0.5% NP-40, 0.5% sodium deoxycholate, 1 mM EDTA, 10 mM Tris, pH 8.1), and three times with 1 ml of buffer 4 (50 mM NaCl, 50 mM Tris, pH 7.4). After the last wash, beads were resuspended in 35 ml of SDS sample buffer saturated with biotin (250 mM Tris, pH 6.8, 0.57 M β-mercaptoethanol, 8% SDS, 40% glycerol) and boiled at 95 °C for 10 min. Purified proteins were separated on SDS–PAGE gel (NP0321BOX; ThermoFisher), stained with Coomassie dye (24615; ThermoFisher), and excised for mass spectrometry analysis.

Gel fractions were submitted to the Proteomics Facility at the Fred Hutchinson Cancer Research Center for mass spectrometry analysis. Briefly, desalted peptide samples were analyzed by liquid chromatography–electrospray ionization tandem mass spectrometry with a Thermo Scientific Easy-nLC II nano HPLC system coupled to a hybrid Orbitrap Elite ETD mass spectrometer using an instrument configuration as described (Yi *et al.*, 2003). In-line desalting was accomplished by using a reversed-phase trap column packed with Magic C_{18}AQ (5-μm 200-Å resin; Michrom Bioresources, Auburn, CA), followed by peptide separations on a reversed-phase column packed with Magic resin and then directly mounted on the electrospray ion source.

Data analysis was performed using Proteome Discoverer 1.4 (Thermo Scientific, San Jose, CA). The data were searched against a Uniprot human database that included common contaminants. Sequest HT was used for database searching, and Percolator was used for scoring. Data acquired from the Orbitrap Elite were processed to generate normalized spectral count values for each protein. Similar to previously published techniques, each protein's spectral counts were divided by the total number of spectral counts for that sample and then divided by the protein's molecular weight (Horton *et al.*, 2015). The resulting value was multiplied by 10^6 and $\log_{10}$-transformed to yield a score for each protein. Protein groups that had the same gene names (e.g., different isoforms or fragments of a larger protein) were combined to decrease redundancies in the analysis. Proteins or arrays were hierarchically clustered on the basis of an uncentered Pearson correlation using Cluster 3.0 and visualized using Java TreeView, as described previously (Horton *et al.*, 2015).

Human bioinformatics studies

To analyze survival as a function of transcriptomic data in human breast cancer patients, we used an online tool (www.kmplot.com; Győrffy *et al.*, 2013). The Affymetrix ID for paxillin was 201087_at. Briefly, the KMplot tool employs gene expression data and relapse-free and overall survival information from the Gene Expression Omnibus, the European Genome-Phenome Archive, and The Cancer Genome Atlas (TCGA) from >4000 patients. To analyze the effect of specific genes in survival, patient samples were split into two groups by predefined metrics for calculating quantile expression. Affymetrix transcriptome data for a user-selected probe were analyzed in KMplot by autoselecting the best cutoff of gene expression, computing the median of expression over the entire database, and analyzing all

patient subtypes as long as they were lymph-node positive in the 2014 TCGA data set. All suggested quality controls were implemented (Györffy *et al.*, 2013).

Reverse-phase protein array (RPPA) data from TCGA patients were analyzed using an online tool (www.cbioportal.org; Gao *et al.*, 2013). Patients were separated into those with paxillin gene amplification, mRNA up-regulation, or protein up-regulation; and those without significant changes in paxillin at the gene, mRNA, or protein level. These two patient groups were then compared for differences in activated and phosphorylated signaling proteins (including Src phosphorylation at tyrosine 416) via previously conducted RPPA arrays.

Statistics

Statistical analysis for two groups was performed with an unpaired, two-tailed Student's *t* test or Wilcoxon rank sum test where appropriate. For multiple comparisons, an analysis of variance test and Holm–Bonferroni *t* test were performed. Calculations were implemented in MATLAB, Python, and Prism.

ACKNOWLEDGMENTS

We thank Micah Dembo and Qingzong Tseng for providing TFM software and assistance, Allan Bradley for the hyperactive piggyBac transposase, Harold Moses for the PyMT Flox3 lines, Zena Werb for the Met1 cell line, Lisa Jones and the Proteomics Facility at the Fred Hutchinson Cancer Research Center for assistance with the protein identification studies, and Eva Huang and Gabriela Lomeli at Stanford University for assistance with the BioID assay and quantification. We thank members of the Weaver, Dunn, Odde, and Lammerding groups for helpful discussions and technical insights. The trainee work was supported by a Department of Defense National Defense Science and Engineering Graduate Fellowship to M.G.R., the National Science Foundation Graduate Research Fellowship Program to A.H.M., L.S.P., A.L.M., G.O., and A.C.C., a 3M Science and Technology Doctoral Fellowship to L.S.P., and a Canadian Institutes of Health Research Postdoctoral Fellowship to F.K. Funding was also provided by National Institutes of Health Grants R01-HL082792 to J.L., R01-CA172986 and U54-CA210190 to D.J.O., R01-GM112998-01 to A.R.D., R01-CA192914, CA174929, and U01-CA202241-01 to V.M.W., and 1U54 CA210184-01 to V.M.W. and J.L. In addition, this work was supported by Department of Defense Breast Cancer Research Program Scholar Expansion Award BC122990 to V.M.W. and Breakthrough Award BC150580 to J.L. and National Science Foundation Grant CBET-1254846 to J.L. This work was performed in part at the Cornell NanoScale Facility, which is supported by National Science Foundation Grant ECCS-15420819.

REFERENCES

Acerbi I, Cassereau L, Dean I, Shi Q, Au A, Park C, Chen YY, Liphardt J, Hwang ES, Weaver VM (2015). Human breast cancer invasion and aggression correlates with ECM stiffening and immune cell infiltration. Integr Biol (Camb) 7, 1120–1134.

Aceto N, Bardia A, Miyamoto DT, Donaldson MC, Wittner BS, Spencer JA, Yu M, Pely A, Engstrom A, Zhu H, *et al.* (2014). Circulating tumor cell clusters are oligoclonal precursors of breast cancer metastasis. Cell 158, 1110–1122.

Allen JL, Cooke ME, Alliston T (2012). ECM stiffness primes the TGFβ pathway to promote chondrocyte differentiation. Mol Biol Cell 23, 3731–3742.

Bae YH, Mui KL, Hsu BY, Liu S-L, Cretu A, Razinia Z, Xu T, Puré E, Assoian RK (2014). A FAK-Cas-Rac-lamellipodin signaling module transduces extracellular matrix stiffness into mechanosensitive cell cycling. Sci Signal 7, ra57.

Bangasser BL, Rosenfeld SS, Odde DJ (2013). Determinants of maximal force transmission in a motor-clutch model of cell traction in a compliant microenvironment. Biophys J 105, 581–592.

Batra N, Burra S, Siller-Jackson AJ, Gu S, Xia X, Weber GF, DeSimone D, Bonewald LF, Lafer EM, Sprague E, *et al.* (2012). Mechanical stress-activated integrin α5β1 induces opening of connexin 43 hemichannels. Proc Natl Acad Sci USA 109, 3359–3364.

Bianchi-Smiraglia A, Kunnev D, Limoge M, Lee A, Beckerle MC, Bakin AV (2013). Integrin-β5 and zyxin mediate formation of ventral stress fibers in response to transforming growth factor β. Cell Cycle 12, 3377–3389.

Borowsky AD, Namba R, Young LJT, Hunter KW, Hodgson JG, Tepper CG, McGoldrick ET, Muller WJ, Cardiff RD, Gregg JP (2005). Syngeneic mouse mammary carcinoma cell lines: two closely related cell lines with divergent metastatic behavior. Clin Exp Metastasis 22, 47–59.

Bravo-Cordero JJ, Hodgson L, Condeelis J (2012). Directed cell invasion and migration during metastasis. Curr Opin Cell Biol 24, 277–283.

Buckley ST, Medina C, Davies AM, Ehrhardt C (2012). Cytoskeletal rearrangement in TGF-β1-induced alveolar epithelial-mesenchymal transition studied by atomic force microscopy and high-content analysis. Nanomed Nanotechnol Biol Med 8, 355–364.

Butcher DT, Alliston T, Weaver VM (2009). A tense situation: forcing tumour progression. Nat Rev Cancer 9, 108–122.

Carisey A, Tsang R, Greiner AM, Nijenhuis N, Heath N, Nazgiewicz A, Kemkemer R, Derby B, Spatz J, Ballestrem C (2013). Vinculin regulates the recruitment and release of core focal adhesion proteins in a force-dependent manner. Curr Biol 23, 271–281.

Cassereau L, Miroshnikova YA, Ou G, Lakins J, Weaver VM (2015). A 3D tension bioreactor platform to study the interplay between ECM stiffness and tumor phenotype. J Biotechnol 193, 66–69.

Chaffer CL, Weinberg RA (2011). A perspective on cancer cell metastasis. Science 331, 1559–1564.

Chan CE, Odde DJ (2008). Traction dynamics of filopodia on compliant substrates. Science 322, 1687–1691.

Chang AC, Mekhdjian AH, Morimatsu M, Denisin AK, Pruitt BL, Dunn AR (2016). Single molecule force measurements in living cells reveal a minimally tensioned integrin state. ACS Nano 10, 10745–10752.

Charras G, Sahai E (2014). Physical influences of the extracellular environment on cell migration. Nat Rev Mol Cell Biol 15, 813–824.

Chaudhuri O, Gu L, Darnell M, Klumpers D, Bencherif SA, Weaver JC, Huebsch N, Mooney DJ (2015). Substrate stress relaxation regulates cell spreading. Nat Commun 6, 6364.

Cheung KJ, Ewald AJ (2014). Illuminating breast cancer invasion: diverse roles for cell-cell interactions. Curr Opin Cell Biol 30, 99–111.

Cheung KJ, Gabrielson E, Werb Z, Ewald AJ (2013). Collective invasion in breast cancer requires a conserved basal epithelial program. Cell 155, 1639–1651.

Cheung KJ, Padmanaban V, Silvestri V, Schipper K, Cohen JD, Fairchild AN, Gorin MA, Verdone JE, Pienta KJ, Bader JS, *et al.* (2016). Polyclonal breast cancer metastases arise from collective dissemination of keratin 14-expressing tumor cell clusters. Proc Natl Acad Sci USA 113, 201508541.

Cosgrove BD, Gilbert PM, Porpiglia E, Mourkioti F, Lee SP, Corbel SY, Llewellyn ME, Delp SL, Blau HM (2014). Rejuvenation of the muscle stem cell population restores strength to injured aged muscles. Nat Med 20, 255–264.

Cox S, Rosten E, Monypenny J, Jovanovic-Talisman T, Burnette DT, Lippincott-schwartz J, Jones GE, Heintzmann R (2011). Bayesian localization microscopy reveals nanoscale podosome dynamics. Nat Methods 9, 195–200.

Craene B, Berx G (2013). Regulatory networks defining EMT during cancer initiation and progression. Nat Rev Cancer 13, 97–110.

Darling EM, Zauscher S, Block JA, Guilak F (2007). A thin-layer model for viscoelastic, stress-relaxation testing of cells using atomic force microscopy: do cell properties reflect metastatic potential. Biophys J 92, 1784–1791.

Davidson PM, Denais C, Bakshi MC, Lammerding J (2014). Nuclear deformability constitutes a rate-limiting step during cell migration in 3-D environments. Cell Mol Bioeng 7, 293–306.

Davidson PM, Sliz J, Isermann P, Denais C, Lammerding J (2015). Design of a microfluidic device to quantify dynamic intra-nuclear deformation during cell migration through confining environments. Integr. Biol (Camb) 7, 1534–1546.

Denais CM, Gilbert RM, Isermann P, McGregor AL, te Lindert M, Weigelin B, Davidson PM, Friedl P, Wolf K, Lammerding J (2016). Nuclear envelope rupture and repair during cancer cell migration. Science 352, 353–358.
Deramaudt TB, Dujardin D, Noulet F, Martin S, Vauchelles R, Takeda K, Ronde P (2014). Altering FAK-paxillin interactions reduces adhesion, migration and invasion processes. PLoS One 9, e92059.
Discher DE, Janmey P, Wang Y-L (2005). Tissue cells feel and respond to the stiffness of their substrate. Science 310, 1139–1143.
Dong J-M, Tay FP-L, Swa HL-F, Gunaratne J, Leung T, Burke B, Manser E, Hall A, Zhao Z, Manser E, *et al.* (2016). Proximity biotinylation provides insight into the molecular composition of focal adhesions at the nanometer scale. Sci Signal 9, rs4.
Doyle AD, Petrie RJ, Kutys ML, Yamada KM (2013). Dimensions in cell migration. Curr Opin Cell Biol 25, 642–649.
DuFort C, Paszek M (2014). Nanoscale cellular imaging with scanning angle interference microscopy. Methods Cell Biol 123, 235–252.
DuFort CC, Paszek MJ, Weaver VM (2011). Balancing forces: architectural control of mechanotransduction. Nat Rev Mol Cell Biol 12, 308–319.
Egeblad M, Rasch MG, Weaver VM (2010). Dynamic interplay between the collagen scaffold and tumor evolution. Curr Opin Cell Biol 22, 697–706.
Elosegui-Artola A, Bazellières E, Allen MD, Andreu I, Oria R, Sunyer R, Gomm JJ, Marshall JF, Jones JL, Trepat X, *et al.* (2014). Rigidity sensing and adaptation through regulation of integrin types. Nat Mater 13, 631–637.
Elosegui-Artola A, Oria R, Chen Y, Kosmalska A, Perez-Gonzalez C, Castro N, Zhu C, Trepat X, Roca-Cusachs P (2016). Mechanical regulation of a molecular clutch defines force transmission and transduction in response to matrix rigidity. Nat Cell Biol 18, 540–548.
Engler AJ, Griffin MA, Sen S, Bönnemann CG, Sweeney HL, Discher DE (2004). Myotubes differentiate optimally on substrates with tissue-like stiffness: pathological implications for soft or stiff microenvironments. J Cell Biol 166, 877–887.
Fischer KR, Durrans A, Lee S, Sheng J, Li F, Wong STC, Choi H, El Rayes T, Ryu S, Troeger J, *et al.* (2015). Epithelial-to-mesenchymal transition is not required for lung metastasis but contributes to chemoresistance. Nature 527, 472–476.
Friedl P, Alexander S (2011). Cancer invasion and the microenvironment: plasticity and reciprocity. Cell 147, 992–1009.
Friedl P, Locker J, Sahai E, Segall JE (2012). Classifying collective cancer cell invasion. Nat Cell Biol 14, 777–783.
Friedl P, Wolf K (2003). Tumour-cell invasion and migration: diversity and escape mechanisms. Nat Rev Cancer 3, 362–374.
Gaggioli C, Hooper S, Hidalgo-Carcedo C, Grosse R, Marshall JF, Harrington K, Sahai E (2007). Fibroblast-led collective invasion of carcinoma cells with differing roles for RhoGTPases in leading and following cells. Nat Cell Biol 9, 1392–1400.
Gao J, Aksoy BA, Dogrusoz U, Dresdner G, Gross B, Sumer SO, Sun Y, Jacobsen A, Sinha R, Larsson E, *et al.* (2013). Integrative analysis of complex cancer genomics and clinical profiles using the cbioportal. Sci Signal 6, pl1.
Ghibaudo M, Saez A, Trichet L, Xayaphoummine A, Browaeys J, Silberzan P, Buguin A, Ladoux B (2008). Traction forces and rigidity sensing regulate cell functions. Soft Matter 4, 1836.
Gillespie DT (1977). Exact stochastic simulation of coupled chemical reactions. J Phys Chem 81, 2340–2361.
Gonzalez-Nieves R, Desantis AI, Cutler ML (2013). Rsu1 contributes to regulation of cell adhesion and spreading by PINCH1-dependent and -independent mechanisms. J Cell Commun Signal 7, 279–293.
Grashoff C, Hoffman BD, Brenner MD, Zhou R, Parsons M, Yang MT, McLean MA, Sligar SG, Chen CS, Ha T, *et al.* (2010). Measuring mechanical tension across vinculin reveals regulation of focal adhesion dynamics. Nature 466, 263–266.
Győrffy B, Surowiak P, Budczies J, Lánczky A (2013). Online survival analysis software to assess the prognostic value of biomarkers using transcriptomic data in non-small-cell lung cancer. PLoS One 8, e82241.
Hannigan G, AA Troussard, Dedhar S (2005). Integrin-linked kinase: a cancer therapeutic target unique among its ILK. Nat Rev Cancer 5, 51–63.
Harada T, Swift J, Irianto J, Shin JW, Spinler KR, Athirasala A, Diegmiller R, Dingal PCDP, Ivanovska IL, Discher DE (2014). Nuclear lamin stiffness is a barrier to 3D migration, but softness can limit survival. J Cell Biol 204, 669–682.
Hidalgo-Carcedo C, Hooper S, Chaudhry SI, Williamson P, Harrington K, Leitinger B, Sahai E (2010). Collective cell migration requires suppression of actomyosin at cell–cell contacts mediated by DDR1 and the cell polarity regulators Par3 and Par6. Nat Cell Biol 13, 49–58.
Hoffman BD, Grashoff C, MA Schwartz (2011). Dynamic molecular processes mediate cellular mechanotransduction. Nature 475, 316–323.
Horton ER, Byron A, Askari JA, Ng DHJ, Millon-Frémillon A, Robertson J, Koper EJ, Paul NR, Warwood S, Knight D, *et al.* (2015). Definition of a consensus integrin adhesome and its dynamics during adhesion complex assembly and disassembly. Nat Cell Biol 17, 1577–1587.
Hu YS, Nan X, Sengupta P, Lippincott-Schwartz J, Cang H (2013). Accelerating 3B single-molecule super-resolution microscopy with cloud computing. Nat Methods 10, 96–97.
Huveneers S, Truong H, Danen HJ (2007). Integrins: signaling, disease, and therapy. Int J Radiat Biol 83, 743–751.
Jaalouk DE, Lammerding J (2009). Mechanotransduction gone awry. Nat Rev Mol Cell Biol 10, 63–73.
Jansen KA, Bacabac RG, Piechocka IK, Koenderink GH (2013). Cells actively stiffen fibrin networks by generating contractile stress. Biophys J 105, 2240–2251.
Johnson KR, Leight JL, Weaver VM (2007). Demystifying the effects of a three-dimensional microenvironment in tissue morphogenesis. Methods Cell Biol 83, 547–583.
Johnson RH, Chien FL, Bleyer A (2013). Incidence of breast cancer with distant involvement among women in the United States, 1976 to 2009. J Am Med Assoc 309, 800–805.
Jolly MK, Boareto M, Huang B, Jia D, Lu M, Ben-Jacob E, Onuchic JN, Levine H (2015). Implications of the hybrid epithelial/mesenchymal phenotype in metastasis. Front Oncol 5, 155.
Jolly MK, Tripathi SC, Jia D, Mooney SM, Celiktas M, Hanash SM, Mani SA, Pienta KJ, Ben-Jacob E, Levine H (2016). Stability of the hybrid epithelial/mesenchymal phenotype. Oncotarget 7, 27067–27084.
Jung HY, Fattet L, Yang J (2015). Molecular pathways: linking tumor microenvironment to epithelial-mesenchymal transition in metastasis. Clin Cancer Res 21, 962–968.
Kai F, Laklai H, Weaver V (2016). Force matters: biomechanical regulation of cell invasion and migration in disease. Trends Cell Biol 26, 486–497.
Kraning-Rush CM, Califano JP, Reinhart-King CA (2012). Cellular traction stresses increase with increasing metastatic potential. PLoS One 7, e32572.
Lakins JN, Chin AR, Weaver VM (2012). Exploring the link between human embryonic stem cell organization and fate using tension-calibrated extracellular matrix functionalized polyacrylamide gels. Methods Mol Biol 916, 317–350.
Laklai H, Miroshnikova YA, Pickup MW, Collisson EA, Kim GE, Barrett AS, Hill RC, Lakins JN, Schlaepfer DD, Mouw JK, *et al.* (2016). Genotype tunes pancreatic ductal adenocarcinoma tissue tension to induce matricellular fibrosis and tumor progression. Nat Med 22, 497–505.
Lamouille S, Xu J, Derynck R (2014). Molecular mechanisms of epithelial-mesenchymal transition. Nat Rev Mol Cell Biol 15, 178–196.
Lautscham LA, Kämmerer C, Lange JR, Kolb T, Mark C, Schilling A, Strissel PL, Strick R, Gluth C, Rowat AC, *et al.* (2015). Migration in confined 3D environments is determined by a combination of adhesiveness, nuclear volume, contractility, and cell stiffness. Biophys J 109, 900–913.
Lee J, Abdeen AA, Tang X, Saif TA, Kilian KA (2015). Geometric guidance of integrin mediated traction stress during stem cell differentiation. Biomaterials 69, 174–183.
Legate KR, Montañez E, Kudlacek O, Fässler R (2006). ILK, PINCH and parvin: the tIPP of integrin signalling. Nat Rev Mol Cell Biol 7, 20–31.
Levental KR, Yu H, Kass L, Lakins JN, Egeblad M, Erler JT, Fong SFT, Csiszar K, Giaccia A, Weninger W, *et al.* (2009). Matrix crosslinking forces tumor progression by enhancing integrin signaling. Cell 139, 891–906.
Lobbezoo DJA, van Kampen RJW, Voogd AC, Dercksen MW, van den Berkmortel F, Smilde TJ, van de Wouw AJ, Peters FPJ, van Riel JMGH, Peters NAJB, *et al.* (2015). Prognosis of metastatic breast cancer: are there differences between patients with de novo and recurrent metastatic breast cancer? Br J Cancer 112, 1445–1451.
Loessner D, Stok KS, Lutolf MP, Hutmacher DW, Clements JA, Rizzi SC (2010). Bioengineered 3D platform to explore cell-ECM interactions and drug resistance of epithelial ovarian cancer cells. Biomaterials 31, 8494–8506.
Longati P, Jia X, Eimer J, Wagman A, Witt M-R, Rehnmark S, Verbeke C, Toftgård R, Löhr M, Heuchel RL (2013). 3D pancreatic carcinoma spheroids induce a matrix-rich, chemoresistant phenotype offering a better model for drug testing. BMC Cancer 13, 95.
Lu P, Weaver VM, Werb Z (2012). The extracellular matrix: a dynamic niche in cancer progression. J Cell Biol 196, 395–406.
Manning CS, Hooper S, Sahai EA (2015). Intravital imaging of SRF and Notch signalling identifies a key role for EZH2 in invasive melanoma cells. Oncogene 34, 4320–4332.

Massagué J, Obenauf AC (2016). Metastatic colonization by circulating tumour cells. Nature 529, 298–306.
McGrail DJ, Mezencev R, Kieu QMN, McDonald JF, Dawson MR (2015). SNAIL-induced epithelial-to-mesenchymal transition produces concerted biophysical changes from altered cytoskeletal gene expression. FASEB J 29, 1280–1289.
Mierke CT, Frey B, Fellner M, Herrmann M, Fabry B (2011). Integrin α5β1 facilitates cancer cell invasion through enhanced contractile forces. J Cell Sci 124, 369–383.
Morimatsu M, Mekhdjian AH, Adhikari AS, Dunn AR (2013). Molecular tension sensors report forces generated by single integrin molecules in living cells. Nano Lett 13, 3985–3989.
Morimatsu M, Mekhdjian AH, Chang AC, Tan SJ, Dunn AR (2015). Visualizing the interior architecture of focal adhesions with high-resolution traction maps. Nano Lett 15, 2220–2228.
Mouw JK, Yui Y, Damiano L, Bainer RO, Lakins JN, Acerbi I, Ou G, Wijekoon AC, Levental KR, Gilbert PM, *et al.* (2014). Tissue mechanics modulate microRNA-dependent PTEN expression to regulate malignant progression. Nat Med 20, 360–367.
Munevar S, Wang Y-L, Dembo M (2001). Traction force microscopy of migrating normal and H-ras transformed 3T3 fibroblasts. Biophys J 80, 1744–1757.
Nguyen DX, Bos PD, Massagué J (2009). Metastasis: from dissemination to organ-specific colonization. Nat Rev Cancer 9, 274–284.
Nguyen-Ngoc KV, Cheung KJ, Brenot A, Shamir ER, Gray RS, Hines WC, Yaswen P, Werb Z, Ewald AJ (2012). ECM microenvironment regulates collective migration and local dissemination in normal and malignant mammary epithelium. Proc Natl Acad Sci USA 109, E2595–E2604.
Osborne LD, Li GZ, How T, O'Brien ET, Blobe GC, Superfine R, Mythreye K (2014). TGF-β regulates LARG and GEF-H1 during EMT to affect stiffening response to force and cell invasion. Mol Biol Cell 25, 3528–3540.
Paluch EK, Nelson CM, Biais N, Fabry B, Moeller J, Pruitt BL, Wollnik C, Kudryasheva G, Rehfeldt F, Federle W (2015). Mechanotransduction: use the force(s). BMC Biol 13, 47.
Pang MF, Siedlik MJ, Han S, Stallings-Mann M, Radisky DC, Nelson CM (2016). Tissue stiffness and hypoxia modulate the integrin-linked kinase ilk to control breast cancer stem-like cells. Cancer Res 76, 5277–5287.
Pasapera AM, Schneider IC, Rericha E, Schlaepfer DD, Waterman CM (2010). Myosin II activity regulates vinculin recruitment to focal adhesions through FAK-mediated paxillin phosphorylation. J Cell Biol 188, 877–890.
Paszek MJ, DuFort CC, Rubashkin MG, Davidson MW, Thorn KS, Liphardt JT, Weaver VM (2012). Scanning angle interference microscopy reveals cell dynamics at the nanoscale. Nat Methods 9, 825–827.
Paszek MJ, Weaver VM (2004). The tension mounts: mechanics meets morphogenesis and malignancy. J Mammary Gland Biol Neoplasia 9, 325–342.
Paszek MJ, Zahir N, Johnson KR, Lakins JN, Rozenberg GI, Gefen A, Reinhart-King CA, Margulies SS, Dembo M, Boettiger D, *et al.* (2005). Tensional homeostasis and the malignant phenotype. Cancer Cell 8, 241–254.
Pathak A, Kumar S (2012). Independent regulation of tumor cell migration by matrix stiffness and confinement. Proc Natl Acad Sci USA 109, 10334–10339.
Persad S, Dedhar S (2003). The role of integrin-linked kinase (ILK) in cancer progression. Cancer Metastasis Rev 22, 375–384.
Pickup MW, Laklai H, Acerbi I, Owens P, Gorska AE, Chytil A, Aakre M, Weaver VM, Moses HL (2013). Stromally derived lysyl oxidase promotes metastasis of transforming growth factor-β-deficient mouse mammary carcinomas. Cancer Res 73, 5336–5346.
Pickup MW, Mouw JK, Weaver VM (2014). The extracellular matrix modulates the hallmarks of cancer. EMBO Rep 15, 1243–1253.
Plotnikov SV, Pasapera AM, Sabass B, Waterman CM (2012). Force fluctuations within focal adhesions mediate ECM-rigidity sensing to guide directed cell migration. Cell 151, 1513–1527.
Provenzano PP, Inman DR, Eliceiri KW, Beggs HE, Keely PJ (2008). Mammary epithelial-specific disruption of focal adhesion kinase retards tumor formation and metastasis in a transgenic mouse model of human breast cancer. Am J Pathol 173, 1551–1565.
Przybyla L, Muncie JM, Weaver VM (2016). Mechanical control of epithelial-to-mesenchymal transitions in development and cancer. Annu Rev Cell Dev Biol 32, 527–554.
Qian B-Z, Li J, Zhang H, Kitamura T, Zhang J, Campion LR, Kaiser EA, Snyder LA, Pollard JW (2011). CCL2 recruits inflammatory monocytes to facilitate breast-tumour metastasis. Nature 475, 222–225.
Quail DF, Joyce JA (2013). Microenvironmental regulation of tumor progression and metastasis. Nat Med 19, 1423–1437.
Ross TD, Coon BG, Yun S, Baeyens N, Tanaka K, Ouyang M, Schwartz MA (2013). Integrins in mechanotransduction. Curr Opin Cell Biol 25, 613–618.
Roussos ET, Balsamo M, Alford SK, Wyckoff JB, Gligorijevic B, Wang Y, Pozzuto M, Stobezki R, Goswami S, Segall JE, *et al.* (2011). Mena invasive (MenaINV) promotes multicellular streaming motility and transendothelial migration in a mouse model of breast cancer. J Cell Sci 124, 2120–2131.
Roux KJ, Kim DI, Raida M, Burke B (2012). A promiscuous biotin ligase fusion protein identifies proximal and interacting proteins in mammalian cells. J Cell Biol 196, 801–810.
Rowe RG, Weiss SJ (2008). Breaching the basement membrane: who, when and how? Trends Cell Biol 18, 560–574.
Rubashkin MG, Cassereau L, Bainer R, DuFort CC, Yui Y, Ou G, Paszek MJ, Davidson MW, Chen YY, Weaver VM (2014a). Force engages vinculin and promotes tumor progression by enhancing PI3K activation of phosphatidylinositol (3,4,5)-triphosphate. Cancer Res 74, 4597–4611.
Rubashkin MG, Ou G, Weaver VM (2014b). Deconstructing signaling in three dimensions. Biochemistry 53, 2078–2090.
Saha K, Keung AJ, Irwin EF, Li Y, Little L, Schaffer D V, Healy KE (2008). Substrate modulus directs neural stem cell behavior. Biophys J 95, 4426–4438.
Sahai E (2007). Illuminating the metastatic process. Nat Rev Cancer 7, 737–749.
Schaller MD (2001). Paxillin: a focal adhesion-associated adaptor protein. Oncogene 20, 6459–6472.
Schedin P, Keely PJ (2011). Mammary gland ECM remodeling, stiffness, and mechanosignaling in normal development and tumor progression. Cold Spring Harb Perspect Biol 3, 1–22.
Schiller HB, Hermann M-R, Polleux J, Vignaud T, Zanivan S, Friedel CC, Sun Z, Raducanu A, Gottschalk K-E, Théry M, *et al.* (2013). β1- and αv-class integrins cooperate to regulate myosin II during rigidity sensing of fibronectin-based microenvironments. Nat Cell Biol 15, 625–636.
Schneider D, Baronsky T, Pietuch A, Rother J, Oelkers M, Fichtner D, Wedlich D, Janshoff A (2013). Tension monitoring during epithelial-to-mesenchymal transition links the switch of phenotype to expression of moesin and cadherins in NMuMG cells. PLoS One 8, e80068.
Serrano I, McDonald PC, Lock FE, Dedhar S (2012). Role of the integrin-linked kinase (ILK)/Rictor complex in TGFβ-1-induced epithelial–mesenchymal transition (EMT). Oncogene 32, 50–60.
Sulzmaier FJ, Jean C, Schlaepfer DD (2014). FAK in cancer: mechanistic findings and clinical applications. Nat Rev Cancer 14, 598–610.
Swaminathan V, Mythreye K, Tim O'Brien E, Berchuck A, Blobe GC, Superfine R (2011). Mechanical stiffness grades metastatic potential in patient tumor cells and in cancer cell lines. Cancer Res 71, 5075–5080.
Taube JH, Herschkowitz JI, Komurov K, Zhou AY, Gupta S, Yang J, Hartwell K, Onder TT, Gupta PB, Evans KW, *et al.* (2010). Core epithelial-to-mesenchymal transition interactome gene-expression signature is associated with claudin-low and metaplastic breast cancer subtypes. Proc Natl Acad Sci USA 107, 15449–15454.
Taylor-Weiner H, Ravi N, Engler AJ (2015). Traction forces mediated by integrin signaling are necessary for definitive endoderm specification. J Cell Sci 128, 1961–1968.
Telerman A, Amson R (2009). The molecular programme of tumour reversion: the steps beyond malignant transformation. Nat Rev Cancer 9, 206–216.
Thoelking G, Reiss B, Wegener J, Oberleithner H, Pavenstaedt H, Riethmuller C (2010). Nanotopography follows force in TGF-beta1 stimulated epithelium. Nanotechnology 21, 265102.
Tsai JH, Donaher JL, Murphy DA, Chau S, Yang J (2012). Spatiotemporal regulation of epithelial-mesenchymal transition is essential for squamous cell carcinoma metastasis. Cancer Cell 22, 725–736.
Tseng Q, Duchemin-Pelletier E, Deshiere A, Balland M, Guillou H, Filhol O, Théry M (2012). Spatial organization of the extracellular matrix regulates cell-cell junction positioning. Proc Natl Acad Sci USA 109, 1506–1511.
Tumbarello DA, Brown MC, Hetey SE, Turner CE (2005). Regulation of paxillin family members during epithelial-mesenchymal transformation: a putative role for paxillin delta. J Cell Sci 118, 4849–4863.
Turner CE (2000). Paxillin interactions. J Cell Sci 113, 4139–4140.
Weaver VM, Lelièvre S, Lakins JN, Chrenek MA, Jones JCR, Giancotti F, Werb Z, Bissell MJ (2002). Beta4 integrin-dependent formation of polarized three-dimensional architecture confers resistance to

apoptosis in normal and malignant mammary epithelium. Cancer Cell 2, 205–216.
Webb DJ, Donais K, Whitmore LA, Thomas SM, Turner CE, Parsons JT, Horwitz AF (2004). FAK–Src signalling through paxillin, ERK and MLCK regulates adhesion disassembly. Nat Cell Biol 6, 154–161.
Wei SC, Fattet L, Tsai JH, Guo Y, Pai VH, Majeski HE, Chen AC, Sah RL, Taylor SS, Engler AJ, *et al*. (2015). Matrix stiffness drives epithelial-mesenchymal transition and tumour metastasis through a TWIST1-G3BP2 mechanotransduction pathway. Nat Cell Biol 17, 678–688.
Weigelt B, Peterse JL, van't Veer LJ (2005). Breast cancer metastasis: markers and models. Nat Rev Cancer 5, 591–602.
White DE, Cardiff RD, Dedhar S, Muller WJ (2001). Mammary epithelial-specific expression of the integrin-linked kinase (ILK) results in the induction of mammary gland hyperplasias and tumors in transgenic mice. Oncogene 20, 7064–7072.
White DE, Kurpios NA, Zuo D, Hassell JA, Blaess S, Mueller U, Muller WJ (2004). Targeted disruption of beta1-integrin in a transgenic mouse model of human breast cancer reveals an essential role in mammary tumor induction. Cancer Cell 6, 159–170.
Winograd-Katz SE, Fässler R, Geiger B, Legate KR (2014). The integrin adhesome: from genes and proteins to human disease. Nat Rev Mol Cell Biol 15, 273–288.
Wolf K, te Lindert M, Krause M, Alexander S, te Riet J, Willis AL, Hoffman RM, Figdor CG, Weiss SJ, Friedl P (2013). Physical limits of cell migration: control by ECM space and nuclear deformation and tuning by proteolysis and traction force. J Cell Biol 201, 1069–1084.
Wolfenson H, Bershadsky A, Henis YI, Geiger B (2011). Actomyosin-generated tension controls the molecular kinetics of focal adhesions. J Cell Sci 124, 1425–1432.
Wolfenson H, Lavelin I, Geiger B (2013). Dynamic regulation of the structure and functions of integrin adhesions. Dev Cell 24, 447–458.
Yao M, Goult BT, Chen H, Cong P, Sheetz MP, Yan J (2014). Mechanical activation of vinculin binding to talin locks talin in an unfolded conformation. Sci Rep 4, 4610.
Ye X, Tam WL, Shibue T, Kaygusuz Y, Reinhardt F, Ng Eaton E, Weinberg RA (2015). Distinct EMT programs control normal mammary stem cells and tumour-initiating cells. Nature 525, 256–260.
Yeung T, Georges PC, Flanagan LA, Marg B, Ortiz M, Funaki M, Zahir N, Ming W, Weaver V, Janmey PA (2005). Effects of substrate stiffness on cell morphology, cytoskeletal structure, and adhesion. Cell Motil Cytoskeleton 60, 24–34.
Yi EC, Lee H, Aebersold R, Goodlett DR (2003). A microcapillary trap cartridge-microcapillary high-performance liquid chromatography electrospray ionization emitter device capable of peptide tandem mass spectrometry at the attomole level on an ion trap mass spectrometer with automated routine operatio. Rapid Commun Mass Spectrom 17, 2093–2098.
Yilmaz M, Christofori G (2009). EMT, the cytoskeleton, and cancer cell invasion. Cancer Metastasis Rev 28, 15–33.
Yoshigi M, Hoffman LM, Jensen CC, Yost HJ, Beckerle MC (2005). Mechanical force mobilizes zyxin from focal adhesions to actin filaments and regulates cytoskeletal reinforcement. J Cell Biol 171, 209–215.
Yu JA, Deakin NO, Turner CE (2009). Paxillin-kinase-linker tyrosine phosphorylation regulates directional cell migration. Mol Biol Cell 20, 4706–4719.
Yu JA, Deakin NO, Turner CE (2010). Emerging role of paxillin-PKL in regulation of cell adhesion, polarity and migration. Cell Adhes Migr 4, 342–347.
Yusa K, Zhou L, Li MA, Bradley A, Craig NL (2011). A hyperactive piggyBac transposase for mammalian applications. Proc Natl Acad Sci USA 108, 1531–1536.
Zaidel-Bar R, Milo R, Kam Z, Geiger B (2006). A paxillin tyrosine phosphorylation switch regulates the assembly and form of cell-matrix adhesions. J Cell Sci 120, 137–148.
Zamir E, Katz BZ, Aota S, Yamada KM, Geiger B, Kam Z (1999). Molecular diversity of cell-matrix adhesions. J Cell Sci 112, 1655–1669.
Zheng X, Carstens JL, Kim J, Scheible M, Kaye J, Sugimoto H, Wu C-C, LeBleu VS, Kalluri R (2015). Epithelial-to-mesenchymal transition is dispensable for metastasis but induces chemoresistance in pancreatic cancer. Nature 527, 525–530.